International Journal of Physical Sciences

Volume 10 Number 13 16 July, 2015

ISSN 1992-1950

Academic Journals

ABOUT IJPS

The **International Journal of Physical Sciences (IJPS)** is published weekly (one volume per year) by Academic Journals.

International Journal of Physical Sciences (IJPS) is an open access journal that publishes high-quality solicited and unsolicited articles, in English, in all Physics and chemistry including artificial intelligence, neural processing, nuclear and particle physics, geophysics, physics in medicine and biology, plasma physics, semiconductor science and technology, wireless and optical communications, materials science, energy and fuels, environmental science and technology, combinatorial chemistry, natural products, molecular therapeutics, geochemistry, cement and concrete research, metallurgy, crystallography and computer-aided materials design. All articles published in IJPS are peer-reviewed.

Contact Us

Editorial Office: ijps@academicjournals.org

Help Desk: helpdesk@academicjournals.org

Website: http://www.academicjournals.org/journal/IJPS

Submit manuscript online http://ms.academicjournals.me/

Editorial Board

International Journal of Physical Sciences

Table of Contents: Volume 10 Number 13, 16 July, 2015

ARTICLES

academicJournals

Vol. 10(13), pp. 378-384, 16 July, 2015
DOI: 10.5897/IJPS2015.4351
Article Number: 67CC74754066
ISSN 1992 - 1950

http://www.academicjournals.org/IJPS

International Journal of Physical Sciences

Full Length Research Paper

Consistency of electrical analogy approach in the prediction of through thickness thermal conductivity of fiber reinforced plastic (FRP) composites with orientation of the square unit cell

Srinivasa Rao T.[1]*, Sambasiva Rao G.[2] and Uma Maheswar Gowd B.[3]

[1]VNR Vignana Jyothi Institute of Engineering and Technology, Hyderabad-500089, India.
[2]Sir C R Reddy College of Engineering, Eluru-534006, India.
[3]JNT University Anantapuramu-515002, India.

Received 19 April, 2015; Accepted 1June, 2015

From the literature, it is found that two different criteria were followed for the prediction of transverse thermal conductivity (K_2) of fiber reinforced plastic (FRP) composites. In the first criterion, the internal anisotropy of the lamina is assumed negligible and K_2 is estimated using simple Fourier's law of 1-D heat conduction applied to representative volume element (RVE). Whereas in the second approach, an electrical analogy method is followed. To estimate the effect of internal anisotropy, through thickness thermal conductivity (K_3) of an FRP lamina is determined by both the approaches through finite element method for an RVE in the auxiliary plane. The problem is modeled in ANSYS 15 software. In the present paper studies are made for various volume fractions (0.1-0.75) and for various angles (20°-90°) made by the section plane with the fiber axis. It is observed that the through thickness thermal conductivity is consistent in the second approach, whereas in the first approach there is considerable variation (max 8.7%) with the orientation of the unit cell.

Key words: Through thickness thermal conductivity, finite element method (FEM), unit cell orientation.

INTRODUCTION

From the literature, it is observed that the transverse thermal conductivity (K_2) of the lamina depends on many parameters like arrangement of fibers, volume fraction, fiber angle, ratio of fiber conductivity to matrix conductivity, etc. It is found from the literature that there are two different approaches to evaluate the transverse thermal conductivity of composites. In the first approach (A-I), the internal anisotropy of the lamina is not considered and K_2 is estimated using simple Fourier's law of 1-D heat conduction. Some of the worth mentioned studies from this criterion are Perrins et al. (1979), who had published exact analytical and experimental results for K_2 and showed very good agreement between experimental and theoretical studies. Another work using

*Corresponding author. E-mail: talluri_sr5@yahoo.co.in

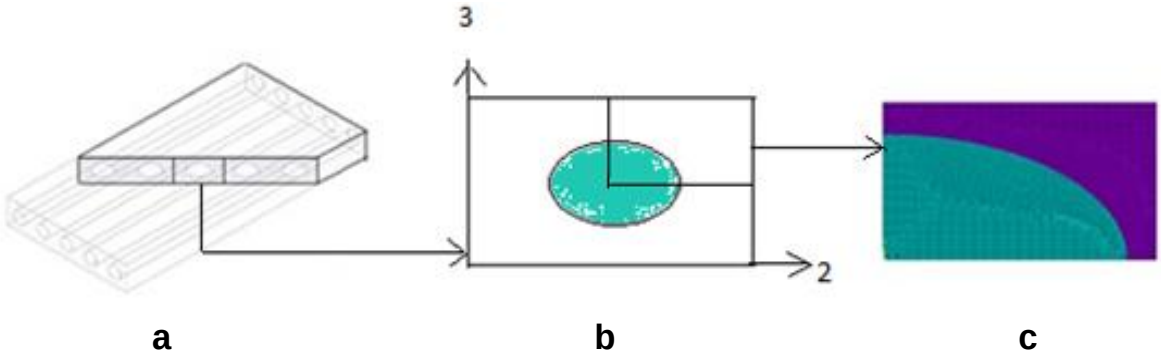

Figure 1. a. Composite b. Unit cell c. FE model.

numerical studies has been made by Lu (1994), who matched the results with Perrins et al. (1979), and stood as source of inspiration for several researches who developed finite element (FE) models for K_2. Sambasiva Rao et al. (2008) developed a 3-D finite element model for circular fibers in square unit cell and compared the results with Perrins et al. (1979) to validate their approach.

In the second approach (A-II), Springer and Tsai (1967), Behrens (1968), Mingqing et al. (2002) considered representative volume element (RVE) as two segments, first one consisting of fiber and matrix arranged normal to the heat flow direction and the second segment being the pure matrix above the first segment, so that the two segments remain parallel to the direction of heat flow, that facilitated them to use Inverse Rule Of Mixtures (IROM) for the first segment and rule of mixures (ROM) for the two segments together. This method allows the heat flow in considered direction only and the usage of 1-D Fourier's law of conduction is justified. Srinivasa Rao et al. (2014a) developed FE models in support of the second criterion.

Prior to Srinivasa Rao et al. (2014b), there was no distinction of the two approaches and the contributors of both methods tried to convince by comparing their results with experimental results, irrespective of the approach they followed. In the present work through thickness thermal conductivity of the composite obtained using both methods are compared. Interestingly, it is observed that K_3 is consistent for all the values of theta in the second approach, whereas it is varying in the first approach.

Finite element model

A schematic diagram of the unidirectional fiber composite is shown in Figure 1a. A representative volume element (RVE) in the form of a square unit cell is adopted for the present analysis. The cross-sectional area of fiber relative to the total cross-sectional area of the unit cell is a measure of the volume of fiber relative to the total volume of the composite (Figure 1b). This fraction is an important parameter in composite materials and is called fiber volume fraction (V_f).

The 1-2-3 coordinate system shown in Figure 1b is used to study the behavior of a unit cell (Direction 1 is along the fiber axis and normal to the plane of 2D figure shown). The isolated unit cell behaves as part of a larger array of unit cells.

It is assumed that the geometry, material and loading of the unit cell are symmetrical with respect to 1-2-3 coordinate system. Therefore, a one forth portion of the unit cell is modeled and the 2-D finite element mesh on one forth portion of the unit cell is shown in Figure 1c. The mesh is generated using six node triangular element (PLANE-35) of ANSYS software, which is quadratic and is best suited along the curved interface between the fiber and the matrix, and has the capability of incorporating isotropic as well as orthotropic materials.

Boundary conditions

Temperature boundary conditions for one-fourth model are as follows: Sides of the unit cell is taken as '2a'.

$$T(x, 0) = T_1; T(x, a) = T_2 \quad (1)$$

The other two faces are subjected to adiabatic boundary conditions.

The effective transverse thermal conductivity is calculated using the equation:

$$q_y = -k_2 \frac{\partial T}{\partial y} \quad (2)$$

Heat flux and the temperature gradient in the above equation are obtained from the finite element solution.

RESULTS AND DISCUSSION

The variation of the normalized through thickness thermal conductivity with respect to theta is shown for both approaches (A-I and A-II) for different volume fractions (Figures 2 to 7). In all the graphs, it is observed that the through thickness thermal conductivity obtained in the second approach (A-II) is constant for all the values of theta at all the volume fractions. Whereas in the first approach (A-I), the normalized through thickness thermal

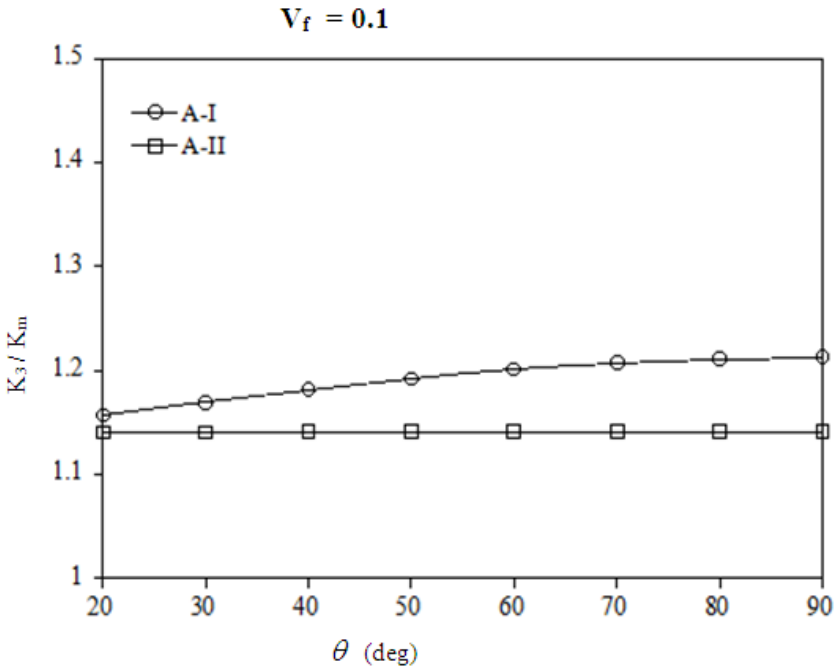

Figure 2. Effect of θ on through thickness conductivity at $V_f = 0.1$.

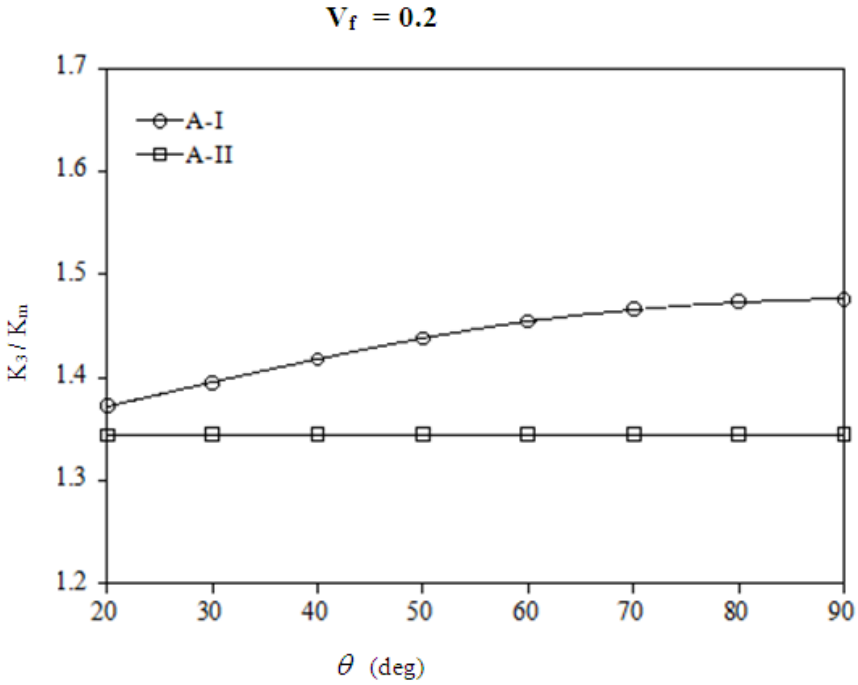

Figure 3. Effect of θ on through thickness conductivity at $V_f = 0.2$.

conductivity increases with theta for all values of V_f. It is also evident from Figures 5 to 7 that the deviation in the results of the two approaches increases with the value of theta at all volume fractions. It is also observed that the deviation increases with V_f at any particular value of theta.

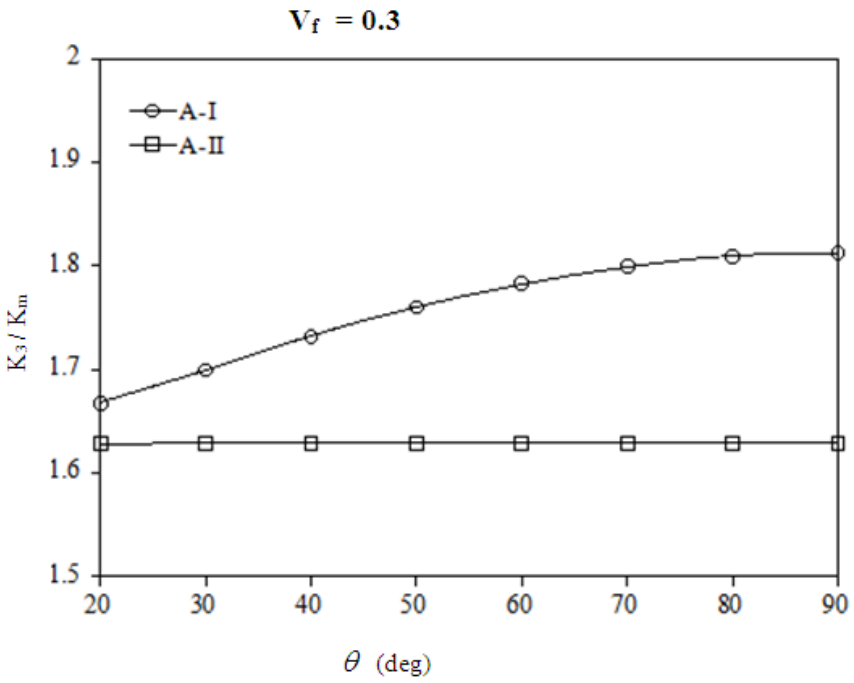

Figure 4. Effect of θ on through thickness conductivity at $V_f = 0.3$.

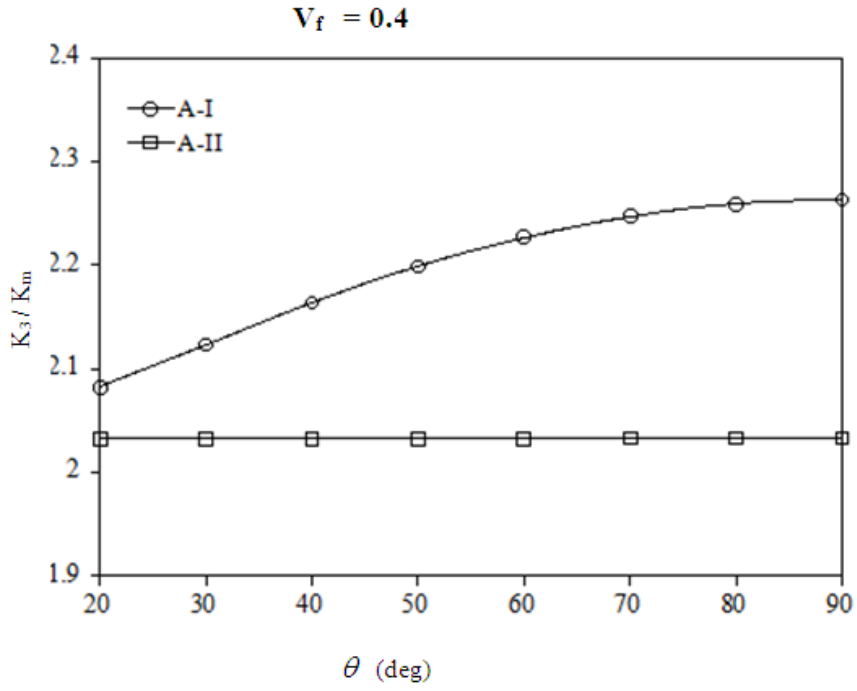

Figure 5. Effect of θ on through thickness conductivity at $V_f = 0.4$.

Figure 8 shows the percentage deviation of through thickness thermal conductivity obtained by the first approach with theta. It is evident from the figure that the percentage deviation of through thickness thermal

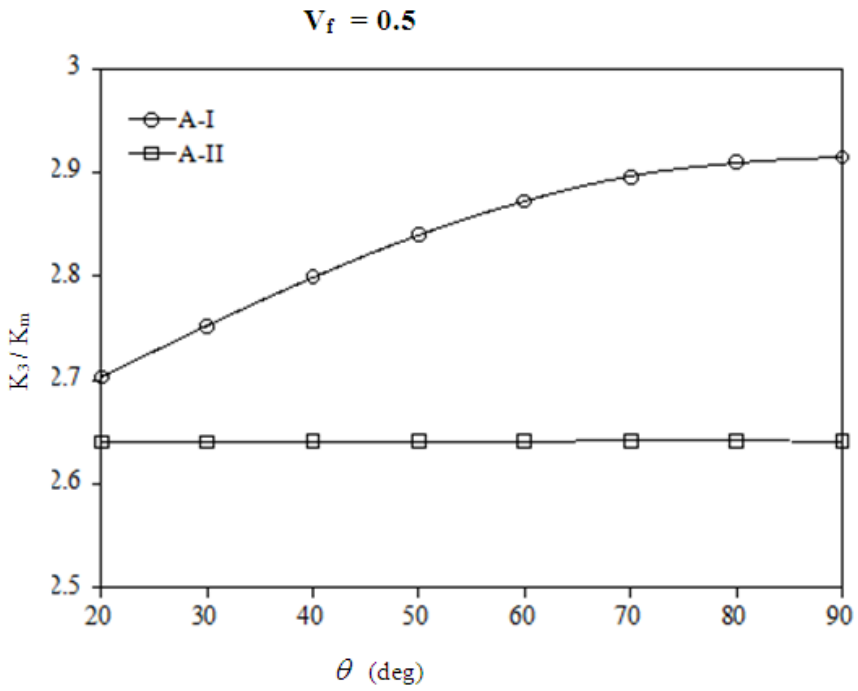

Figure 6. Effect of θ on through thickness conductivity at $V_f = 0.5$.

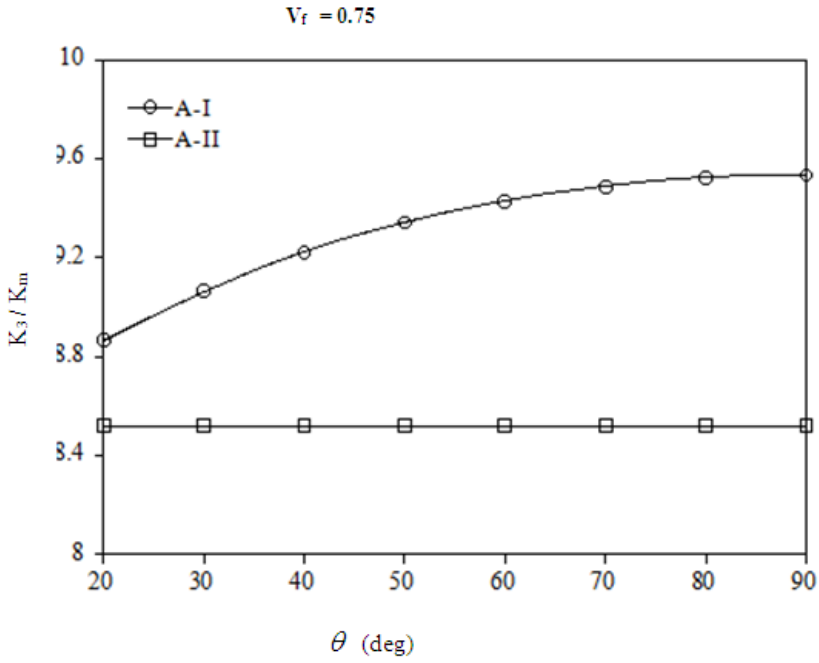

Figure 7. Effect of θ on through thickness conductivity at $V_f = 0.75$.

conductivity is varying from 4.8 to 8.7%. Up to a volume fraction of 0.35, the percentage deviation is showing increasing trend followed by a marginal decrease.

In Figure 9, percentage deviation of through thickness thermal conductivity with reference to second approach at various theta values for $K_f/K_m = 50$ is shown. It is

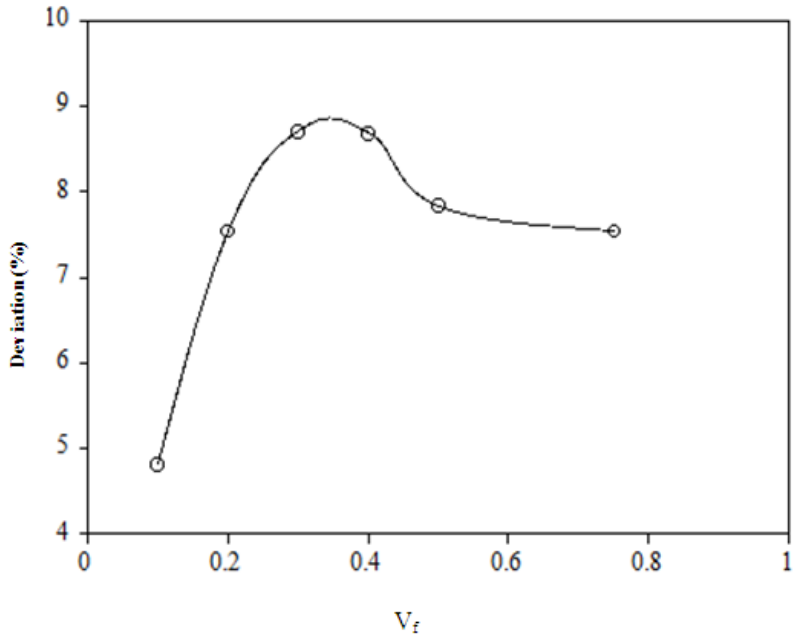

Figure 8. Deviation of K_3 (Approach-I) for $K_f/K_m = 50$ and $\theta = 90°$.

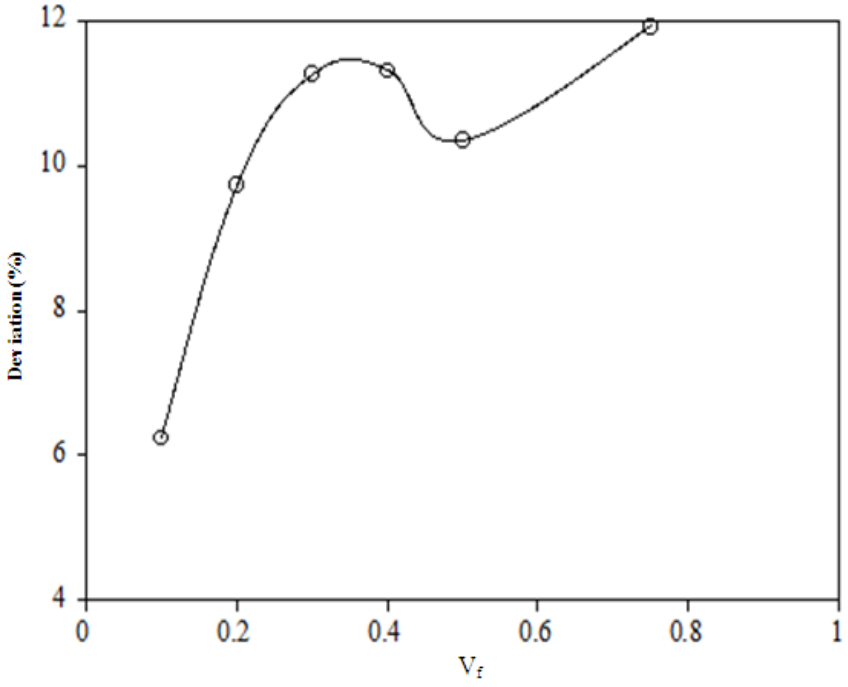

Figure 9. Deviation of K_3 (A-I&A-II) for $K_f/K_m = 50$ and $\theta = 90°$.

observed that the percentage deviation is varying from 6.2 to 11.9%. Initially, the percentage deviation increases up to a volume fraction of 0.35, then decreases up to a volume fraction of 0.5 and then increases steadily beyond $V_f = 0.5$.

The variation in the percentage difference in transverse thermal conductivity with either the theta or the approach is attributed to the presence of internal anisotropy in the first approach.

Conclusions

An attempt is made to compare the through thickness conductivity of FRP composite obtained in two different approaches available in the literature. It is evident from the above results that there is considerable deviation in the results obtained from the two approaches for the range of V_f of 0.1 to 0.75 and $K_f/K_m = 50$. This difference is attributed to the assumption of negligible internal anisotropy in the first approach.

Conflict of Interest

The authors have not declared any conflict of interest.

REFERENCES

Behrens E (1968). Thermal Conductivities of Composite Materials. J. Compos. Mater. 2:2-17. doi: 10.1177/002199836800200101

Mingqing Z, Boming Y, Duanming Z (2002). An Analytical Solution for Transverse Thermal Conductivities of Unidirectional Fibre Composites with Thermal Barrier. J. Phys. D: Appl. Phys. 35:1867-1874. doi:10.1088/0022-3727/35/15/309

Perrins WT, McKenzie DR, McPhedran RC (1979). Transport Properties of Regular Arrays of Cylinders, Proc. Royal society of London. Series A. 369:207-225. DOI: 10.1098/rspa.1979.0160

Sambasiva Rao G, Subramanyam T, Balakrishna Murthy V (2008). 3-D Finite Element Models for the Prediction of Effective Transverse Thermal Conductivity of Unidirectional Fibre Reinforced Composites. Int. J. Appl. Eng. Res. 3(1):99-108.

Lu S-Y (1994). The Effective Thermal Conductivities of Composites with 2-D Arrays of Circular and Square Cylinders. J. Compos. Mater. 29:483-506.

Springer GS, Tsai SW (1967). Thermal Conductivities of Unidirectional Materials. J. Compos. Mater. 1:166-173.

Srinivasa Rao T, Sambasiva Rao G, Uma Maheswar Gowd B (2014a). Finite Element Models for Prediction of Transverse Thermal Conductivity Based on Electrical Analogy, Mechanics of Composites (MechComp2014), Stonybrook, NY, USA. P.178.

Srinivasa Rao T, Sambasiva Rao G, Uma Maheswar Gowd B (2014b). Comparative Study of Different Approaches in the Prediction of Transverse Thermal Conductivity. Procedia Mater. Sci. 6:1879-1883.

academicJournals

Vol. 10(13), pp. 385-390, 16 July, 2015
DOI: 10.5897/IJPS2015.4354
Article Number: 6773C7D54070
ISSN 1992 - 1950

http://www.academicjournals.org/IJPS

International Journal of Physical Sciences

Full Length Research Paper

Optical and structural properties of lead sulphide (PbS) thin films synthesized by chemical method

B. A. Ezekoye[1]*, T. M. Emeakaroha[1], V. A. Ezekoye[1], K. O. Ighodalo[1] and P. O. Offor[2]

[1]Crystal Growth and Characterization Laboratory, Department of Physics and Astronomy, University of Nigeria, Nsukka, Enugu State, Nigeria.
[2]Department of Metallurgical and Materials Engineering, University of Nigeria.

Received 21 April, 2015; Accepted 15 June, 2015

The influence of dip times on the lead sulphide (PbS) thin films deposited on glass slide substrates via chemical bath deposition (CBD) technique using chemical precursors, nitrate $Pb(NO_3)_2$, and thiourea, $(SC(NH_2)_2)$ in alkaline medium at 300 K was investigated. The optical, structural and morphological studies were performed by UV-vis spectophotometry, X-ray diffraction (XRD) and scanning electron microscopy (SEM) respectively. The XRD showed films of cubic (galena), crystalline in nature with the preferential (111) orientation. The optical studies showed films of direct band gaps in the range of 1.59-1.65 eV.

Key words: Lead sulphide, thin films, lead sulphide (PbS), X-Ray diffraction, scanning electron microscope (SEM), bandgap.

INTRODUCTION

Lead sulphide (PbS) is an important IV-VI group chalcogenides semiconductor that has attracted considerable attention in the recent times due to its numerous optical and opto-electronic properties and useful applications in solar cells, optoelectronic devices, photoconductors, sensors and infrared detector devices (Chattarki et al., 2012; Koao et al., 2014; Preetha et al., 2015). PbS thin films has direct optical bandgap that can be changed from 0.39 up to 5.20eV (Koao et al., 2014). PbS thin films have been deposited through various deposition processes such as electrodeposition (Osherov et al., 2007), spray pyrolysis (Rajashree et al., 2014; Thangaraju and Kaliannan, 2000), chemical bath deposition (Koao et al., 2014; Preetha et al., 2015; Garcia-Valenzuela et al., 2013; Fernandez-Lima et al., 2007), and successive ionic layer adsorption and reaction (Puiso et al., 2003; Gulen, 2014; Pawar et al., 2013).

Chemical bath method is a very simple, relatively cost effective, convenient for large area scaling and is used in the deposition of good quality thin films with physical and chemical properties comparable to other methods. In the last decade, there has been a renewed interest in this method, mainly associated with its remarkable success in depositing semiconductor layers in thin film photovoltaic cells. By chemical bath deposition (CBD), the crystallites can be varied by controlling deposition parameters (Abbas et al., 2011). Researchers observed that thermal treating process has effect on the rate of absorptivity of PbS thin films and consequently influence the optical characterization of chemically deposited (Thangaraju and

*Corresponding author. E-mail: benjamin.ezekoye@unn.edu.ng

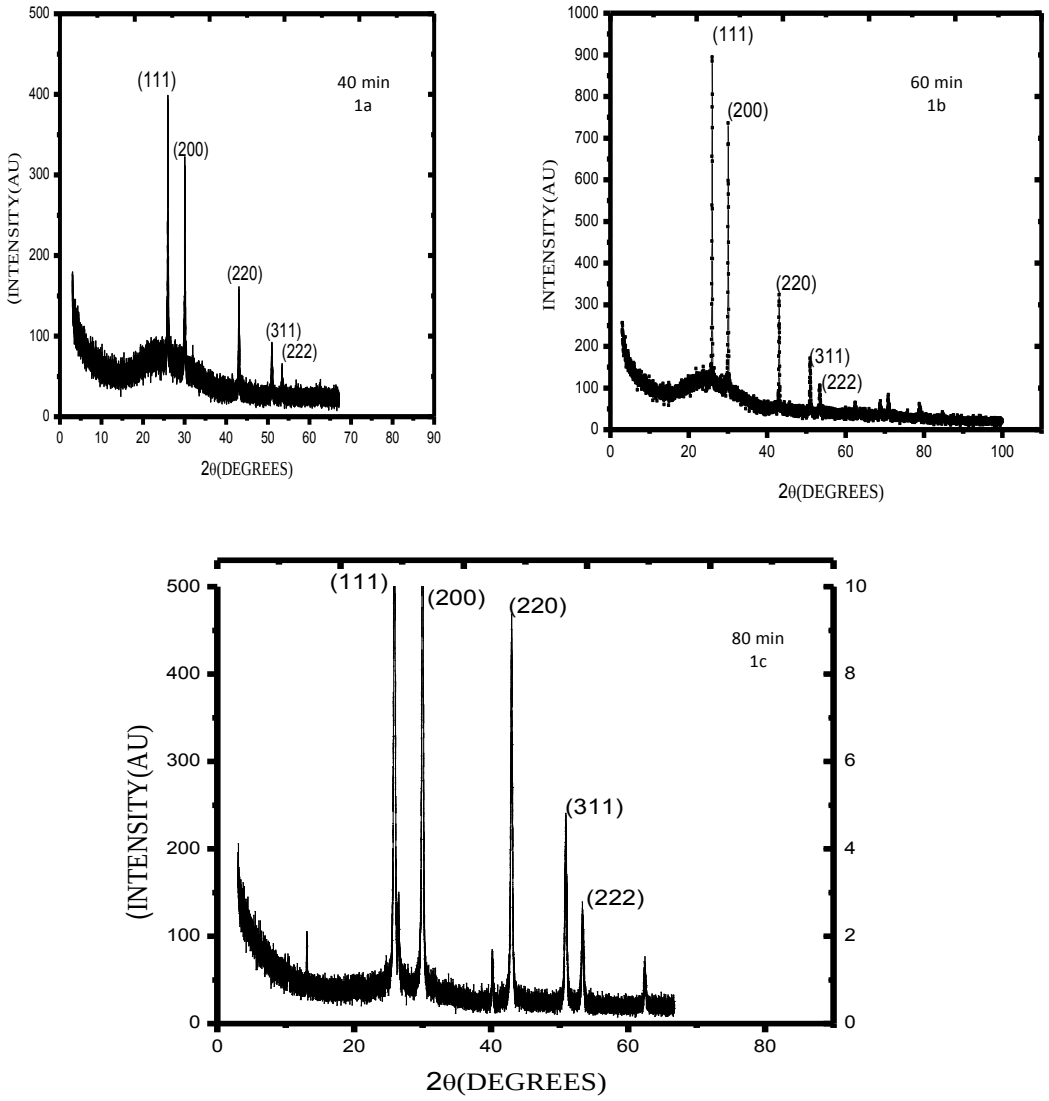

Figure 1. XRD Pattern of CBD PbS Thin Films for (A) 40 min deep time, (B) 60 min and (C) 80 min.

Kaliannan, 2000).

In the present study, the authors investigated the influence of dip times on the lead sulphide (PbS) thin films deposited on glass slide substrates via CBD technique using chemical precursors, nitrate $Pb(NO_3)_2$], and thiourea,$(SC(NH_2)_2)$ in alkaline medium at 300K.

MATERIALS AND METHODS

Lead sulphide thin films were deposited on glass substrate by the chemical bath method. The precursor chemicals were lead nitrate ($Pb(NO_3)_2$), thiourea $(SC(NH_2)_2)$ and sodium hydroxide $NaOH$. Thiourea is used as our sulphide ion source and leads nitrate as our lead ion source. The deposition process is based on slow release of Pb^{2+} and S^{2-} ions in the solution which condensed on the substrate. Lead sulphide were constituted from a solution of 10 ml of 0.1 M lead nitrate ($Pb(NO_3)_2$), 10 ml of 0.8 M thiourea $(SC(NH_2)_2)$, 10 ml of 0.8 M sodium hydroxide ($NaOH$) and distilled water of 40 ml were added to the solution making it total of 70 ml. Cleaned substrates were vertically immersed into the solution and was maintained at room temperature. The substrates were subsequently taken out of the chemical bath after 40, 60 and 80 min dip time, rinsed with distilled water and dried. The resulting films were uniform, homogeneous and well adhered to the substrate with dark surface. The suggested reactions are as follows (Tohidi et al., 2014; Osherov et al., 2007).

$$Pb(NO_3)_2 + 4NaOH \rightarrow [Pb(OH)_4]^{2-} + 4Na^{+} + 2NO^{3-}$$

$$[Pb(OH)_4]^{2-} + SC(NH_2)_2 \rightarrow PbS + 2OH^{-} + CN_2H_2 + 2H_2O$$

RESULTS AND DISCUSSION

Figure 1 shows the X-ray diffraction patterns for PbS thin

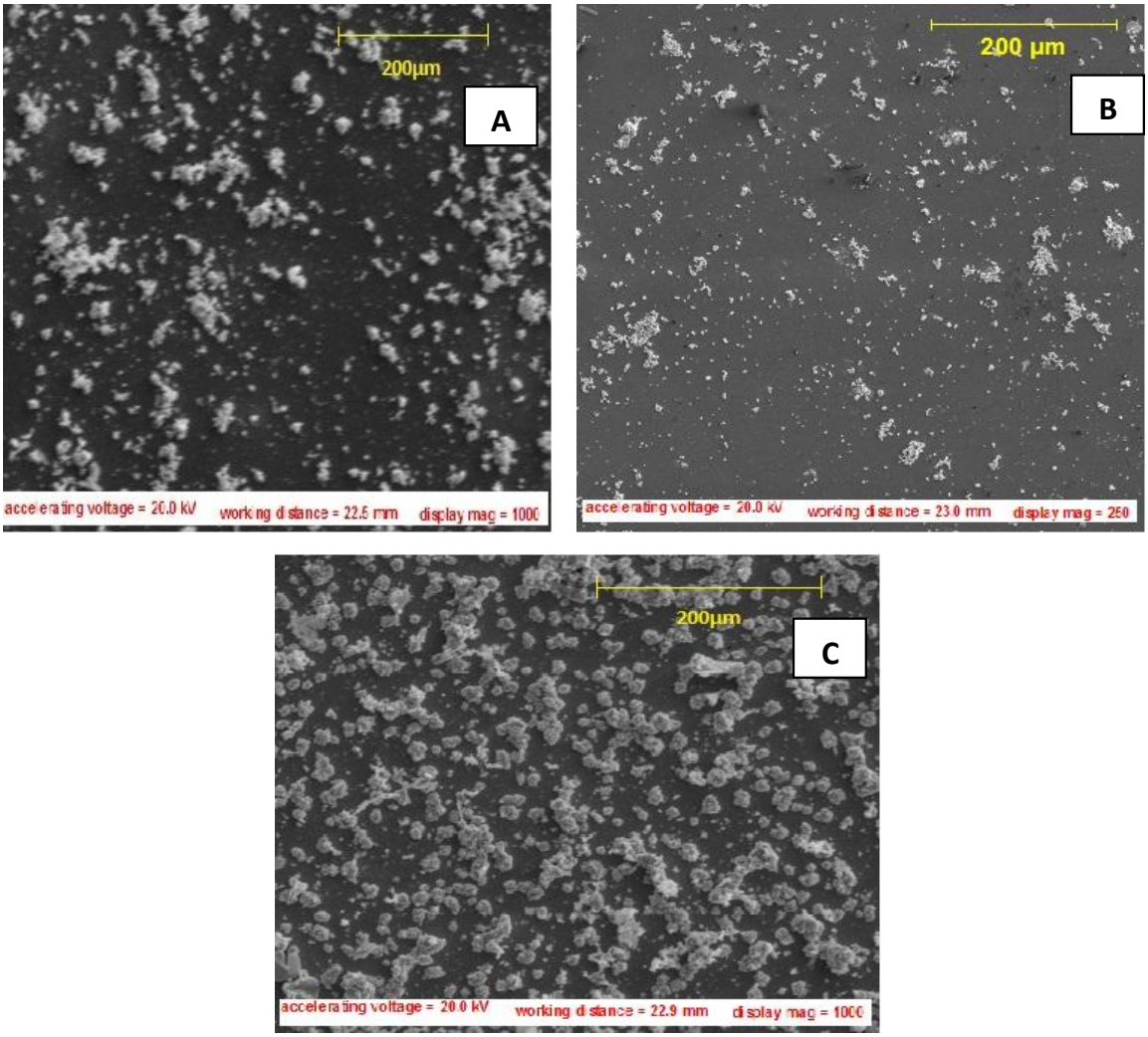

Figure 2. SEM images for PbS deposited thin films for (A) 40 min deep time, (B) 60 min and (C) 80 min.

films according to the standard X-ray diffraction data files with reference No.03-065-0692. The diffraction peaks of the cubic PbS thin films were found at peaks (111), (200), (220), (311), (222), which corresponds to 2θ angles ranging from 25.98-70.95 for all the samples. The as-prepared films have (111) preferential orientation, cubic and polycrystalline in nature and lattice constant 5.9360 Å, with CuKα irradiation (λ=1.5443Å).

The crystalline size of the deposited films for all the samples were calculated using Full Width Half Maximum data (FWHM) and Debye-Scherer formula and their grain size are in within the ranges of (12-27) nm (Chaudhuri et al., 2005; Abbas et al., 2011).

$$D = \frac{0.9\,\lambda}{\beta cos\theta} \quad (1)$$

Where D=Grain Size, λ=is the wavelength of CuKα used, θ=is Bragg's diffraction angle in degrees and β=is Full width at half maximum of the peak in radians.

Figure 2 shows the SEM PbS thin films using CBD method. It shows that the PbS thin films were homogeneous in nature and sparsely packed crystallites which appear to be randomly oriented with irregular and spherical shape of similar sizes distribution for film deposited by CBD. This agrees with other reports of Castillo et al. (2014) and Jana et al. (2008).

Figure 3 shows the plots from optical studies for the absorption measurements carried out in the wavelength range of 200 to 1100 nm. Figure 3a shows the variation of absorbance with wavelength for the deposited PbS thin films at different dip times from 450 to 100 nm. The sample A (40 min) exhibited absorbance with peak of about 0.98 (a.u) corresponding to wavelength of about 480 nm which is in the near infrared region. Sample B (60 min) shows maximum absorbance of about 750 nm at

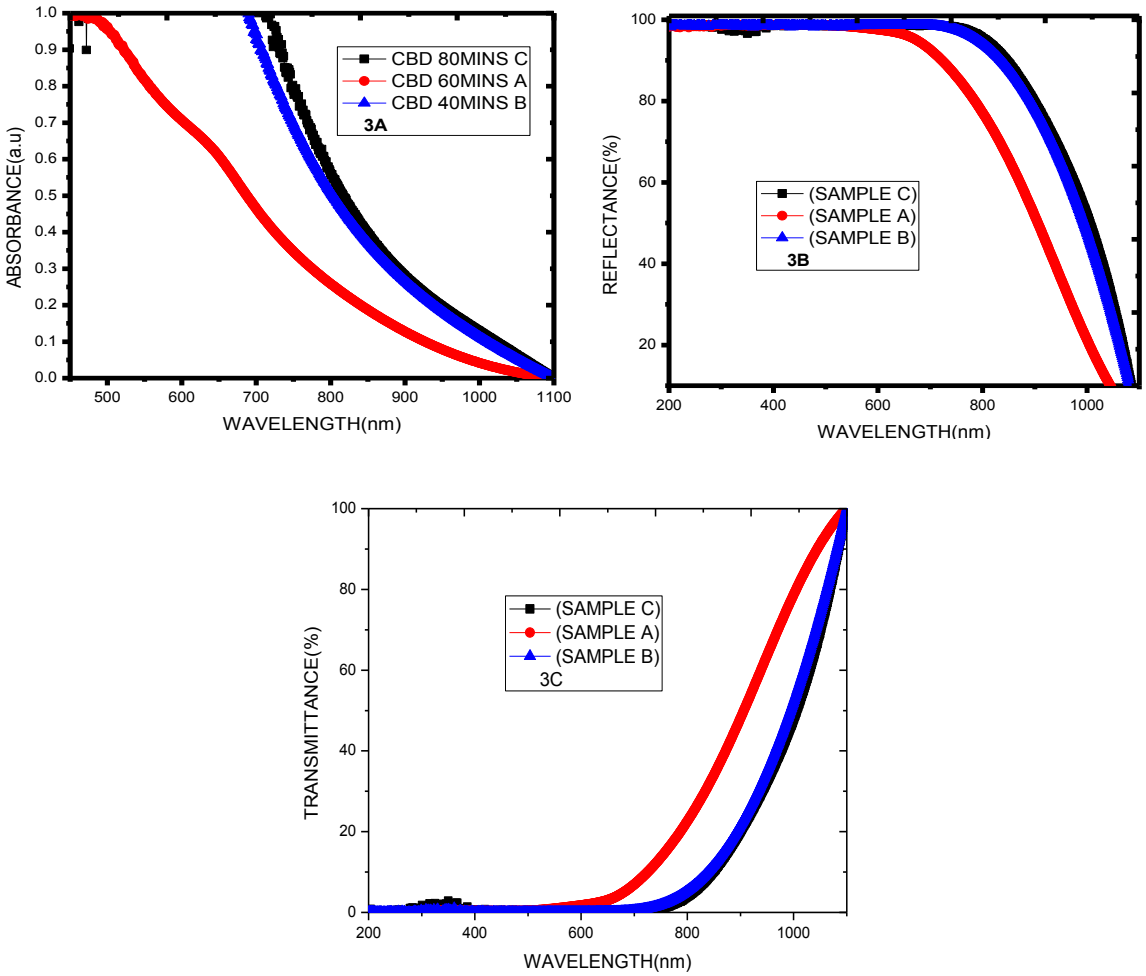

Figure 3. Absorbance, reflectance and transmittance spectra (200-1100 nm) of the PbS CBD deposited thin films.

0.99 (au) in the visible region. Sample C (80 min) shows maximum absorbance with peak of about 0.98 (au) corresponding to wavelength of 760 nm which is also in the near infrared region. The absorbance of the entire sample is about the same (au); this is because of the complexing agent employed during the deposition (Castillo et al., 2014; Abbas et al., 2011; Jana et al., 2008).

Figure 3b shows the reflectance spectra of PbS thin films at different dip times. All the samples show high reflectance in the visible region which rapidly decreased in the near infrared region. This high reflectance and absorbance in the visible region make the thin film good material for anti-reflection coating and also for solar thermal applications, the films can be employed as a solar control coating, also applied in infrared (IR) detectors (Castillo et al., 2014; Abbas et al., 2011; Jana et al., 2008; Larramendi et al., 2001).

Figure 3c shows the transmittance spectra of PbS thin films at different dip times. All the samples show low transmittance in the visible region which rapidly increased in the infrared region. This shows that the reflectance spectra is correct because it is opposite of transmittance. This is done using Equation (2) (Castillo et al., 2014; Abbas et al., 2011).

$$T = \frac{(1-R^2),\exp(-4\pi t/\lambda)}{1-R^2\ \exp(-8\pi t/\lambda)} \quad (2)$$

Where t = thickness and **λ** = wavelength.

The absorption coefficient α associated with the strong absorption region of the film was calculated from absorbance (A) and the thin film thickness (t) which was calculated using the relation below (Manouchehri et al., 2014):

$$\alpha = 2.3026\,A/t \quad (3)$$

The absorption coefficient α was analyzed using the following expression for optical absorption of semiconductors (Manouchehri et al., 2014):

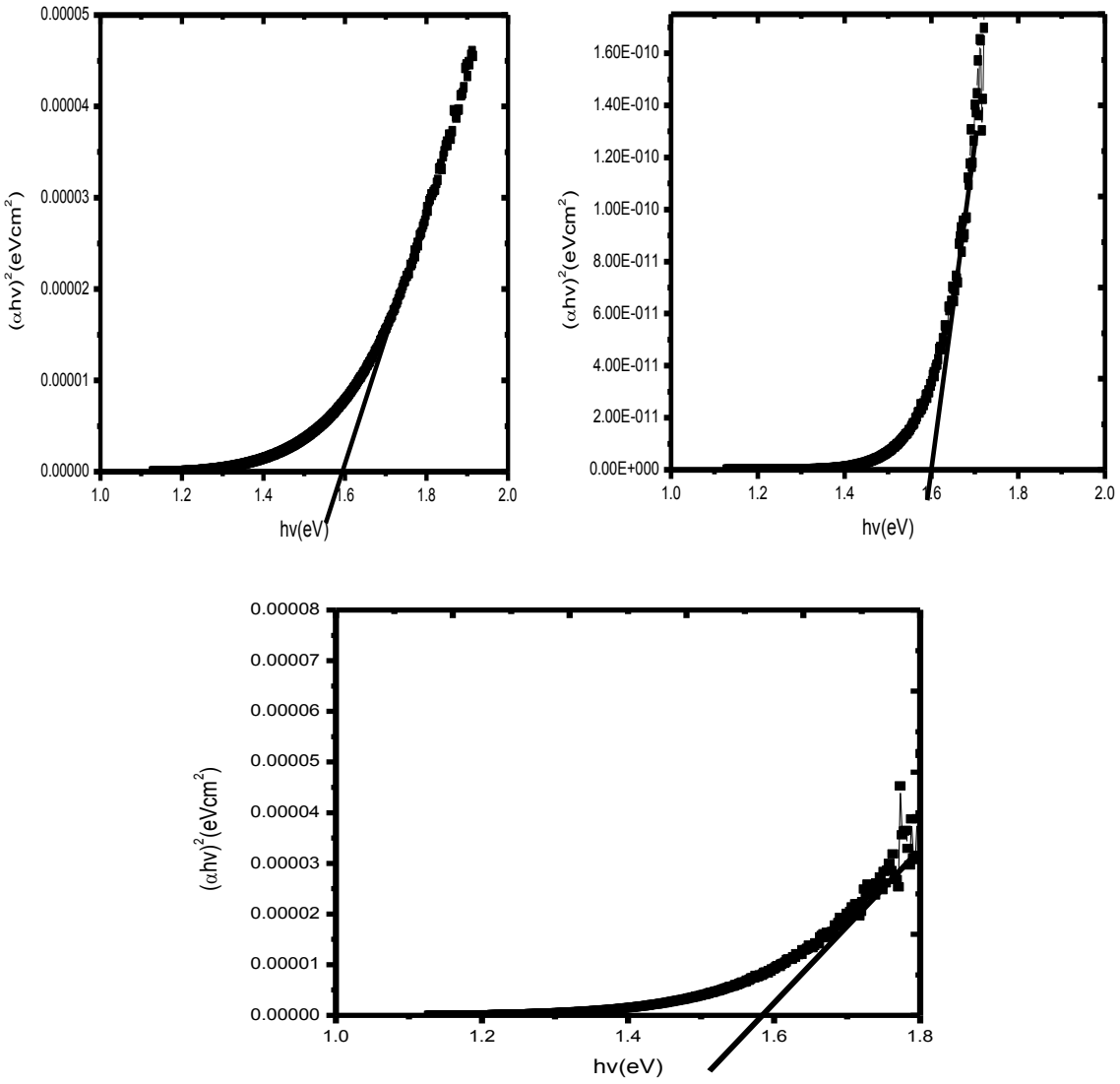

Figure 4. Plots of $(\alpha hv)^2$ versus $h\nu$ for PbS thin films for (A) 40 min deep time, (B) 60 min and (C) 80 min.

$$(\alpha hv) = K(hv - E_g)^{n/2} \quad (4)$$

where K = constant, E_g = energy band gap and n = 1 for allowed direct band gap semiconductor.

Figure 4 shows, Plots of $(\alpha hv)^2$ versus $h\nu$ for PbS thin films at different dip times.

The values obtained for the direct band gap of PbS thin films deposited by chemical bath lies within the range of 1.59-1.65eV. A close observation of the band gap range shows that increase in deposition time increases the band gap.

Figure 5 shows the plot of thickness against the deposition time. The thickness increased with the deposition; time increases (Manouchehri et al., 2014; Abbas et al., 2011), until after 1100 nm and remained almost constant.

Conclusion

Chemical bath deposition (CBD) method has been successfully used to deposit PbS thin films. The optical adsorption, morphological and structural studies of the thin films were carried out. The results obtained from the XRD for the PbS thin films was found to be polycrystalline in nature and grown in cubic crystal structure (galena), with grain sizes of (12 to 27 nm). The properties of high absorbance and high reflectance in the visible region, low absorbance and high reflectance in the near infrared region make the film a good material for anti-reflection coating and for solar thermal applications and infrared (IR) sensors.

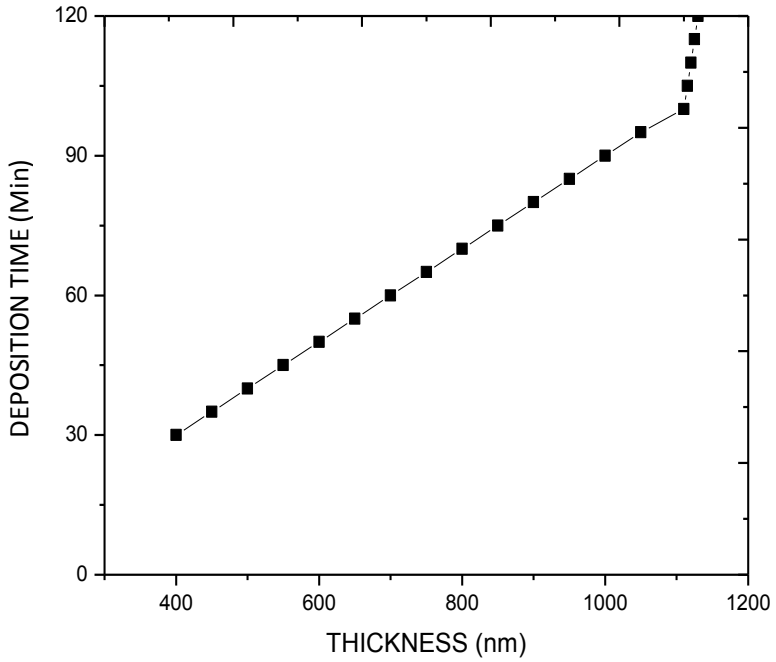

Figure 5. Plot of Deposition time Vs Thickness of PbS thin films.

Conflict of Interest

The authors declare no conflict of interests.

REFERENCES

Abbas MM, Shehab AM, Samuraee AK, Hassah NA (2011). Effect of Deposition Time on the Optical Characteristics of Chemically Deposited Nanostructure PbS Thin Films. Energy. Procedia. 6:241-250. http://dx.doi:10.1016/j.egypro.2011.05.028.

Castillo AC, AmbrosioLázaro RC, Jimenez-Pérez A, MartínezPérez CA, DelaCruzTerrazas EC, Quevedo-López MA (2014). Role of complexing agents in chemical bath deposition of lead sulfide thin films. Mater. Lett. 121:19–21. http://dx.doi:10.1016/j.matlet.2014.01.088.

Chattarki AN, Kamble SS, Deshmukh LP (2012). Role of pH in aqueous alkaline chemical bath deposition of lead sulfide thin films. Mater. Lett. 67:39-41. http://dx.doi:10.1016/j.matlet.2011.08.105.

Chaudhuria T, Sahab TN, Saha P (2005). Deposition of PbS particles from a non-aqueous chemical bath at room temperature. Mater. Lett. 59:2191–2193. http://dx.doi:10.1016/j.matlet.2005.02.064.

Fernandez-Lima FA, Gonz´alez-Alfaro Y, Larramendi EM, Fonseca Filho HD, Maia da Costa MEH, Freire Jr. FL, Prioli R, De Avillez RR, Da Silveira EF, Calzadilla O, De Melo O, Pedrero E, Hern´andez E (2007). Structural characterization of chemically deposited PbS thin films. Mater. Sci. Eng. B. 136:187–192. http//dx.doi:10.1016/j.mseb.2006.09.029.

Garcia-Valenzuela JA, Baez-Gaxiola MR, Sotelo-Lerma M (2013). Chemical bath deposition of PbS thin films on float glass substrates using a $Pb(CH_3COO)_2$–NaOH–$(NH_2)_2CS$–$N(CH_2CH_2OH)_3$–CH_3CH_2OH definite aqueous system and their structural, optical, and electrical/photoelectrical Characterization. Thin Solid Flims. 534:26-131. http://dx.doi.org/10.1016/j.tsf.2013.02.035.

Gülen Y (2014). Characteristics of Ba-Doped PbS Thin Films Prepared by the SILAR Method. Acta Physica Polonica A. 126:763-767. DOI: 10.12693/APhysPolA.126.763.

Jana S, Thapa R, Maity R, Chattopadhyay KK (2008). Optical and dielectric properties of PVA capped nanocrystalline PbS thin films synthesized by chemical bath deposition. Physica E. 40:3121-3126. doi:10.1016/j.physe.2008.04.015.

Koao LF, Dejene FB, Swart HC (2014). Synthesis of PbS nanostructures by chemical bath deposition method. Int. J. Electrochem. Sci. 9:1747-1757.

Larramendi EM, Calzadilla O, Gonz´alez-Arias A, Hern´andez E, Ruiz-Garcia J (2001). Effect of surface structure on photosensitivity in chemically deposited PbS thin films. Thin Solid Films. 389:301-306.

Manouchehri S, Zahmatkesh J, Heidari-Sani M, Barzekar T, Yousefi MH (2014). Refractive index, optical bandgap and oscillator parameters of PbS thin films deposited by CBD technique. Experiment. 26(3):1816-1823.

Osherov A, Ezersky V, Golan Y (2007). The role of solution composition in chemical bath deposition of epitaxial thin films of PbS on GaAs (100). J. Crystal Growth. 308:334–339. http://dx.doi.org /10.1016/j.jcrysgro.2007.07.046.

Pawar SB, Pawar SA, Patil PS, Bhosale PN (2013). Chemosynthesis of PbS thin film by SILAR technique. AIP Conf. Proc. 1536:483-484. http://dx.doi.org/10.1063/1.4810311.

Preetha KC, Deepa K, Dhanya AC, Remadevi TL (2015). Role of complexing agents on chemical bath deposited PbS thin film characterization. Mater. Sci. Eng. 73. http://dx.doi.org/10.1088/1757-899X/73/1/012086.

Puišo J, Lindroos S, Tamulevicius S, Leskelä M, Snitka V (2003).The influence of the pretreatment of Si substrate on the growth of PbS thin films in the SILAR Technique. Solid State Phenomena, 94:261-264. http://dx.doi.org/10.4028/www.scientific.net/SSP.94.261.

Rajashree C, Balu AR, Nagarethinam VS (2014). Substrate temperature effect on the Physical properties of Spray deposited Lead sulfide thin films suitable for solar control coatings. Int. J. Chem. Tech. Res. 6:347-360.

Thangaraju B, Kaliannan P (2000). Spray pyrolytically deposited PbS thin films. Semicond. Sci. Technol. 15:849-853. PII:S0268-1242(00)10001-X.

Tohidi T, Jamshidi-Ghaleh K, Namdar A, RezaAbdi G (2014). Comparative studies on the structural, morphological, optical, and electrical properties of nanocrystalline PbS thin films grown by chemical bath deposition using two different bath compositions. Mater. Sci. Semiconductor Process. 25:197–206. http://dx.doi.org/10.1016/j.mssp.2013.11.028.

academicJournals

Vol. 10(13), pp. 391-402, 16 July, 2015
DOI: 10.5897/IJPS2015.4289
Article Number: 8F9E05354073
ISSN 1992 - 1950

http://www.academicjournals.org/IJPS

International Journal of Physical Sciences

Full Length Research Paper

The generalized projective Riccati equations method and its applications for solving two nonlinear PDEs describing microtubules

Elsayed M. E. Zayed and Khaled A. E. Alurrfi

Department of Mathematics, Faculty of Science, Zagazig University P. O. Box 44519, Zagazig, Egypt.

Received 27 February, 2015; Accepted 10 June, 2015

Microtubules (MTs) are major cytoskeletal proteins. They are hollow cylinders formed by protofilaments (PFs) representing series of proteins known as tubulin dimers. Each dimer is an electric dipole. These diamers are in a straight position within PFs or in radially displaced positions pointing out of cylindrical surface. In this paper, the authors demonstrate how the generalized projective Riccati equations method can be used in the study of the nonlinear dynamics of MTs. To this end, the authors apply this method to construct the exact solutions with parameters for two nonlinear PDEs describing MTs. The first equation describes the model of microtubules as nanobioelectronics transmission lines. The second equation describes the dynamics of radial dislocations in microtubules. As a result, hyperbolic, trigonometric and rational function solutions are obtained. When these parameters are taken as special values, solitary wave solutions are derived from the exact solutions. Comparison between our recent results and the well-known results is given.

Key words: Generalized projective Riccati equations method, models of microtubules (MTs), exact solutions, solitary solutions, trigonometric solutions rational solutions.

INTRODUCTION

In the recent years, investigations of exact solutions to nonlinear partial differential equations (NPDEs) play an important role in the study of nonlinear physical phenomena. Nonlinear wave phenomena appear in various scientific and engineering field, such as fluid mechanics, plasma physics, optical fibers, biology, solid state physics, chemical kinematics, chemical physics and geochemistry. To obtain traveling wave solutions, many powerful methods have been presented, such as the $\exp(-\varphi(\xi))$ expansion method (Hafez et al., 2014), the tanh-sech method (Malfiieiet, 1992; Malfiieiet and Hereman, 1996; Wazwaz, 2004a), extended tanh-method (EL-Wakil and Abdou, 2007; Fan, 2000; Wazwaz, 2007), sine-cosine method (Wazwaz, 2004b, 2005; Yan, 1996), homogeneous balance method (Fan and Zhang, 1998;

*Corresponding author. E-mails: e.m.e.zayed@hotmail.com, alurrfi@yahoo.com.

PACS: 02.30.Jr, 04.20. JB, 05.45.Yv.

Wang, 1996), Jacobi elliptic function method (Dai and Zhang, 2006; Fan and Zhang, 2002; Liu et al., 2001; Zhao et al., 2006), F-expansion method (Abdou, 2007; Ren and Zhang, 2006; Zhang et al., 2006), exp-function method (He and Wu, 2006; Aminikhad et al., 2009), trigonometric function series method (Zhang, 2008), $(\frac{G'}{G})$-expansion method (Zhang et al., 2008; Zayed and Gepreel, 2009; Younis and Zafar, 2014; Younis, 2014a, b; Zayed, 2009; Hayek, 2010), the (G'/G,1/G)-expansion method (Zayed and Hoda Ibrahim, 2013a; Zayed and Alurrfi, 2014a, b, c), the modified simple equation method (Jawad et al., 2010; Zayed, 2011; Zayed and Hoda Ibrahim, 2012, 2013b, 2014 ; Zayed and Arnous, 2012), the first integral method (Moosaei et al., 2011; Bekir and Unsal, 2012; Lu et al., 2010; Feng, 2002), the multiple exp-function algorithm method (Ma et al., 2010; Ma and Zhu, 2012), the transformed rational function method (Ma and Lee, 2009), the Frobenius decomposition technique (Ma et al., 2007), the local fractional variation iteration method (Yang et al., 2013), the local fractional series expansion method (Yang et al., 2013), the generalized projective Riccati equations method (Conte and Musette, 1992; Zayed and Alurrfi, 2014d; Zhang et al., 2001; Yan, 2003; Yomba, 2005), the generalized $(\frac{G'}{G})$-expansion method (Alam and Akbar, 2013; 2014a, b, 2015; Alam et al., 2014a, b, c, d) and so on. Conte and Musette (1992) presented an indirect method to seek more solitary wave solutions of some NPDEs that can be expressed as polynomials in two elementary functions which satisfy a projective Riccati equation (Bountis et al. 1986). Using this method, many solitary wave solutions of many NPDEs are found (Zhang et al., 2001; Bountis et al. 1986). Recently, Yan (2003) developed further Conte and Musette's method by introducing more generalized projective Riccati equations.

The objective of this paper is to apply the generalized projective Riccati equations method to construct the exact solutions for the following two nonlinear PDEs of microtubules (MTs):

(i) The nonlinear PDE describing the nonlinear dynamics of MTs as nanobioelectronics transmission lines:

$$m\frac{\partial^2 z(x,t)}{\partial t^2}-kl^2\frac{\partial^2 z(x,t)}{\partial x^2}-qE-Az(x,t)+Bz^3(x,t)+\gamma\frac{\partial z(x,t)}{\partial t}=0, \quad (1)$$

where $z(x,t)$ is the traveling wave, m is the mass of the dimer, k is a harmonic constant describing the nearest-neighbor interaction between the dimers belonging to the same protofilaments (PFs), l is the MT length, *E* is the magnitude of intrinsic electric field, *q>0* is the excess charge within the dipole, γ is the viscosity coefficient and A,B are positive parameters. The physical details of the derivation of Equation (1) has been discussed in Zekovic et al. (2014) which are omitted here for simplicity. The authors (Zekovic et al., 2014) have used the Jacobi elliptic function method to find the exact solutions of Equation (1).

(ii) The nonlinear PDE describing the nonlinear dynamics of radial dislocations in MTs:

$$I\frac{\partial^2\phi(x,t)}{\partial t^2}-ch^2\frac{\partial^2\phi(x,t)}{\partial x^2}+pH\phi(x,t)-\frac{pH}{6}\phi^3(x,t)+\Gamma\frac{\partial\phi(x,t)}{\partial t}=0, \quad (2)$$

where $\phi(x,t)$ is the corresponding angular displacement when the whole dimer rotates with the angular displacement $\phi(x,t)$, I is the moment of inertia of the single dimer, c stands for inter-dimer bonding interaction within the same protofilaments (PFs), h is the MT length, *p* is the electric dipole moment, H is the magnitude of intrinsic electric field and Γ is the viscosity coefficient. The physical details of the derivation of Equation (2) has been discussed in Zdravkovic et al. (2014) which are omitted here for simplicity. The authors (Zdravkovic et al., 2014) have used the simplest equation method to find the exact solutions of Equation (2).

Description of the generalized projective Riccati equations method

Considering the following NPDE:

$$F(u,u_t,u_x,u_{tt},u_{xt},u_{xx},...)=0, \quad (3)$$

where F is a polynomial in $u(x,t)$ and its partial derivatives, in which the highest order derivatives and nonlinear terms are involved. In the following, the authors give the main steps (Conte and Musette, 1992; Zayed and Alurrfi, 2014d; Zhang et al., 2001; Yan, 2003; Yomba, 2005) of this method.

Step 1. The authors use the wave transformation

$$u(x,t)=u(\xi),\quad \xi=k_1x+\omega t, \quad (4)$$

where k_1, and ω are constants, to reduce Equation (3) to the following ODE:

$$Q(u,u',u'',...)=0, \quad (5)$$

where Q is a polynomial in $u(\xi)$ and its total derivatives, such that $'=\frac{d}{d\xi}$.

Step 2. The authors assume that Equation (5) has the formal solution:

$$u(\xi)=A_0+\sum_{i=1}^{N}\sigma^{i-1}(\xi)\left[A_i\sigma(\xi)+B_i\tau(\xi)\right], \quad (6)$$

where A_0, A_i and B_i are constants to be determined later. The functions $\sigma(\xi)$ and $\tau(\xi)$ satisfy the ODEs:

$$\sigma'(\xi)=\varepsilon\sigma(\xi)\tau(\xi) \quad (7)$$

$$\tau'(\xi)=R+\varepsilon\tau^2(\xi)-\mu\sigma(\xi), \quad \varepsilon=\pm 1, \quad (8)$$

Where

$$\tau^2(\xi)=-\varepsilon\left(R-2\mu\sigma(\xi)+\frac{\mu^2+r}{R}\sigma^2(\xi)\right), \quad (9)$$

where $r=\pm 1$ and R, μ are nonzero constants.

If $R,=\mu=0,$ Equation (5) has the formal solution:

$$u(\xi)=\sum_{i=0}^{N}A_i\tau^i(\xi), \quad (10)$$

where $\tau(\xi)$ satisfies the ODE:

$$\tau'(\xi)=\tau^2(\xi). \quad (11)$$

Step 3. The authors determine the positive integer N in (6) by using the homogeneous balance between the highest-order derivatives and the nonlinear terms in Equation (5).

Step 4. Substitute (6) along with Equations (7) - (9) into Equation (5) or ((10) along with Equation (11) into Equation (5)). Collecting all terms of the same order of $\sigma^j(\xi)\tau^i(\xi)$ $(j=0,1,...;i=0,1)$ (or $\tau^i(\xi)$, $j=0,1,...$). Setting each coefficient to zero, yields a set of algebraic equations which can be solved to find the values of $A_0, A_i, B_i, k_1, \omega, \mu$ and R .

Step 4. It is well known (Yomba, 2005) that Equations (7) and (8) admit the following solutions:

Case 1. When $\varepsilon=-1, r=-1, R>0,$

$$\sigma_1(\xi)=\frac{R\,\mathrm{sech}\left(\sqrt{R}\xi\right)}{\mu\,\mathrm{sech}\left(\sqrt{R}\xi\right)+1}, \quad \tau_1(\xi)=\frac{\sqrt{R}\,\tanh\left(\sqrt{R}\xi\right)}{\mu\,\mathrm{sech}\left(\sqrt{R}\xi\right)+1}, \quad (12)$$

Case 2. When $\varepsilon=-1, r=1, R>0,$

$$\sigma_2(\xi)=\frac{R\,\mathrm{csch}\left(\sqrt{R}\xi\right)}{\mu\,\mathrm{csch}\left(\sqrt{R}\xi\right)+1}, \quad \tau_2(\xi)=\frac{\sqrt{R}\,\coth\left(\sqrt{R}\xi\right)}{\mu\,\mathrm{csch}\left(\sqrt{R}\xi\right)+1}, \quad (13)$$

Case 3. When $\varepsilon=1, r=-1, R>0,$

$$\sigma_3(\xi)=\frac{R\,\sec\left(\sqrt{R}\xi\right)}{\mu\sec\left(\sqrt{R}\xi\right)+1}, \quad \tau_3(\xi)=\frac{\sqrt{R}\,\tan\left(\sqrt{R}\xi\right)}{\mu\sec\left(\sqrt{R}\xi\right)+1}, \quad (14)$$

$$\sigma_4(\xi)=\frac{R\,\csc\left(\sqrt{R}\xi\right)}{\mu\csc\left(\sqrt{R}\xi\right)+1}, \quad \tau_4(\xi)=-\frac{\sqrt{R}\,\cot\left(\sqrt{R}\xi\right)}{\mu\csc\left(\sqrt{R}\xi\right)+1}, \quad (15)$$

Case 4. $R,=\mu=0,$

$$\sigma_5(\xi)=\frac{C}{\xi}, \quad \tau_5(\xi)=\frac{1}{\varepsilon\xi}, \quad (16)$$

where C is nonzero constant.

Step 6. Substituting the values of $A_0, A_i, B_i, k_1, \omega, \mu$ and R. as well as the solutions (12) - (16) into (6) the authors obtain the exact solutions of Equation (3).

APPLICATIONS

In this part, the authors will apply the proposed method described in description of the generalized projective Riccati equations method, to find the exact solutions of the two nonlinear PDEs (1) and (2).

Example 1. Exact solutions of the nonlinear PDE (1) describing the nonlinear dynamics of MTS as nanobioelectronics transmission lines

The authors find the exact wave solutions of Equation (1). To this end, the authors use the transformation (4) to reduce Equation (1) into the following ODE:

$$\alpha\psi''(\xi)-\rho\psi'(\xi)-\psi(\xi)+\psi^3(\xi)-\delta=0, \quad (17)$$

where

$$\alpha=\frac{m\omega^2-kl^2k_1^2}{A}, \rho=\frac{\gamma\omega}{A}, \delta=\frac{qE}{A\sqrt{A/B}}, \quad (18)$$

and

$$z(\xi)=\sqrt{\frac{A}{B}}\psi(\xi). \quad (19)$$

Balancing $\psi''(\xi)$ with $\psi^3(\xi)$ in Equation (17), the

authors get $N=1$. Consequently, the authors have the formal solution of Equation (17) as follows:

$$\psi(\xi)=A_0+A_1\sigma(\xi)+B_1\tau(\xi). \tag{20}$$

where A_0, A_1 and B_1 are constants to be determined later.

Substituting (20) into (17) and using (7) - (9), the left-hand side of Equation (17) becomes a polynomial in $\sigma(\xi)$ and $\tau(\xi)$. Setting the coefficients of this polynomial to be zero, yields the following system of algebraic equations:

$$\sigma^3(\xi):\quad RA_1^3+(\mu^2+r)(2\alpha A_1\varepsilon^2+3A_1B_1^2)=0,$$

$$\sigma^2(\xi):\quad (\mu^2+r)(3A_0B_1^2-\rho B_1\varepsilon)-2R(2\alpha A_1\varepsilon^2+3A_1B_1^2)\mu-\varepsilon\alpha\mu RA_1+3RA_0A_1^2=0,$$

$$\sigma^2(\xi)\tau(\xi):\quad 3RA_1^2B_1+(\mu^2+r)(2\alpha B_1\varepsilon^2+B_1^3)=0,$$

$$\sigma(\xi):\quad -2\mu(3A_0B_1^2-\rho B_1\varepsilon)+R(2\alpha A_1\varepsilon^2+3A_1B_1^2)-A_1+\varepsilon\alpha A_1R+3A_0^2A_1+\rho\mu B_1=0,$$

$$\sigma(\xi)\tau(\xi):\quad -\varepsilon\rho A_1+6A_0A_1B_1-3\varepsilon\alpha\mu B_1-2(2\alpha B_1\varepsilon^2+B_1^3)\mu=0,$$

$$\tau(\xi):\quad 2\alpha B_1\varepsilon R-B_1+3A_0^2B_1+(2\alpha B_1\varepsilon^2+B_1^3)R=0,$$

$$\sigma^0(\xi):\quad R(3A_0B_1^2-\rho B_1\varepsilon)-A_0+A_0^3-\rho RB_1-\delta=0. \tag{21}$$

Case 1. If authors substitute $\varepsilon=-1$ into the algebraic equations (21) and solve them by Maple 14, the following results were realized:

Result 1. The authors have

$$A_0=\pm\frac{\rho}{6}\sqrt{\frac{-2}{\alpha}},\ A_1=0,\ B_1=\pm\sqrt{-2\alpha},\ R=-\frac{\rho^2+6\alpha}{12\alpha^2},\ \mu=0, \tag{22}$$
$$\delta=\pm\frac{\rho(2\rho^2+9\alpha)\sqrt{-2\alpha}}{27\alpha^2}, r=r$$

where $\alpha<0,\ \rho^2+6\alpha<0$.

From (12), (13), (19), (20) and (22), the authors deduce that if $r=-1$, then the exact wave solution was realized:

$$z(\xi)=\pm\sqrt{\frac{-2A}{\alpha B}}\left[\frac{\rho}{6}+\sqrt{-\frac{\rho^2+6\alpha}{12}}\tanh\left(\sqrt{-\frac{\rho^2+6\alpha}{12\alpha^2}}\xi\right)\right], \tag{23}$$

while if $r=1$, then the authors have the exact wave solution

$$z(\xi)=\pm\sqrt{\frac{-2A}{\alpha B}}\left[\frac{\rho}{6}+\sqrt{-\frac{\rho^2+6\alpha}{12}}\coth\left(\sqrt{-\frac{\rho^2+6\alpha}{12\alpha^2}}\xi\right)\right]. \tag{24}$$

Result 2. The authors have

$$A_0=\pm\frac{\rho}{3}\sqrt{\frac{-2}{\alpha}},\ A_1=0,\ B_1=\pm\sqrt{\frac{-2}{\alpha}},\ R=-\frac{\rho^2+6\alpha}{3\alpha^2},\ \mu=\pm\sqrt{-r}, \tag{25}$$
$$\delta=\pm\frac{\rho(2\rho^2+9\alpha)\sqrt{-2\alpha}}{27\alpha^2},$$

where $\alpha<0, r<0,\ \rho^2+6\alpha<0$.

In this case, the authors deduce that if $r=-1$, then the exact wave solution was realized:

$$z(\xi)=\pm\sqrt{\frac{-A}{2\alpha B}}\left[\frac{\rho}{3}+\frac{\sqrt{-\frac{\rho^2+6\alpha}{3}}\tanh\left(\sqrt{-\frac{\rho^2+6\alpha}{3\alpha^2}}\xi\right)}{1\pm\operatorname{sech}\left(\sqrt{-\frac{\rho^2+6\alpha}{3\alpha^2}}\xi\right)}\right]. \tag{26}$$

Result 3. The authors have

$$A_0=\pm\frac{\rho}{3}\sqrt{\frac{-2}{\alpha}},\ A_1=\pm\sqrt{\frac{3\alpha^3(\mu^2+r)}{2(\rho^2+6\alpha)}},\ B_1=\pm\sqrt{\frac{-2}{\alpha}},\ R=-\frac{\rho^2+6\alpha}{3\alpha^2},\ \mu=\mu, \tag{27}$$
$$\delta=\pm\frac{\rho(2\rho^2+9\alpha)\sqrt{-2\alpha}}{27\alpha^2},$$

where $\alpha<0,\ \rho^2+6\alpha<0,\ \mu^2+r>0$.

In this case, the authors deduce that if $r=-1$, then the exact wave solution was realized:

$$z(\xi)=\pm\sqrt{\frac{-A}{2\alpha B}}\left[\frac{\rho}{3}+\sqrt{-\frac{\rho^2+6\alpha}{3}}\right.$$
$$\left.\times\left(\frac{\left(\sqrt{\mu^2-1}\right)\operatorname{sech}\left(\sqrt{-\frac{\rho^2+6\alpha}{3\alpha^2}}\xi\right)+\tanh\left(\sqrt{-\frac{\rho^2+6\alpha}{3\alpha^2}}\xi\right)}{\mu\operatorname{sech}\left(\sqrt{-\frac{\rho^2+6\alpha}{3\alpha^2}}\xi\right)+1}\right)\right], \tag{28}$$

while if $r=1$, then the authors have the exact wave solution

$$z(\xi)=\pm\sqrt{\frac{-A}{2\alpha B}}\left[\frac{\rho}{3}+\sqrt{-\frac{\rho^2+6\alpha}{3}}\right.$$
$$\left.\times\left(\frac{\left(\sqrt{\mu^2+1}\right)\operatorname{csch}\left(\sqrt{-\frac{\rho^2+6\alpha}{3\alpha^2}}\xi\right)+\coth\left(\sqrt{-\frac{\rho^2+6\alpha}{3\alpha^2}}\xi\right)}{\mu\operatorname{csch}\left(\sqrt{-\frac{\rho^2+6\alpha}{3\alpha^2}}\xi\right)+1}\right)\right]. \tag{29}$$

Case 2. If the authors substitute $\varepsilon=1$ and $r=-1$ into the algebraic Equations (21) and solve them by Maple 14, the authors have the following results:

Result 1. The authors have

$$A_0=\mp\frac{\rho}{6}\sqrt{\frac{-2}{\alpha}},\ A_1=0,\ B_1=\pm\sqrt{-2\alpha},\ R=\frac{\rho^2+6\alpha}{12\alpha^2},\ \mu=0, \tag{30}$$
$$\delta=\mp\frac{\rho(2\rho^2+9\alpha)\sqrt{-2\alpha}}{27\alpha^2},$$

where $\alpha<0$, $\rho^2+6\alpha>0$.

From (14), (15), (19), (20) and (30), the authors deduce the following exact wave solutions

$$z(\xi)=\pm\sqrt{\frac{-2A}{\alpha B}}\left[-\frac{\rho}{6}+\sqrt{\frac{\rho^2+6\alpha}{12}}\tan\left(\sqrt{\frac{\rho^2+6\alpha}{12\alpha^2}}\xi\right)\right], \tag{31}$$

or

$$z(\xi)=\mp\sqrt{\frac{-2A}{\alpha B}}\left[\frac{\rho}{6}+\sqrt{\frac{\rho^2+6\alpha}{12}}\cot\left(\sqrt{\frac{\rho^2+6\alpha}{12\alpha^2}}\xi\right)\right]. \tag{32}$$

Result 2. The authors have

$$A_0=\mp\frac{\rho}{3}\sqrt{\frac{-2}{\alpha}},\ A_1=0,\ B_1=\pm\sqrt{\frac{-2}{\alpha}},\ R=\frac{\rho^2+6\alpha}{3\alpha^2},\ \mu=\pm1, \tag{33}$$
$$\delta=\mp\frac{\rho(2\rho^2+9\alpha)\sqrt{-2\alpha}}{27\alpha^2},$$

where $\alpha<0,\ \rho^2+6\alpha>0$.

In this case, the authors deduce the exact wave solutions

$$z(\xi)=\pm\sqrt{\frac{-A}{2\alpha B}}\left[-\frac{\rho}{3}+\frac{\sqrt{\frac{\rho^2+6\alpha}{3}}\tan\left(\sqrt{\frac{\rho^2+6\alpha}{3\alpha^2}}\xi\right)}{1\pm\sec\left(\sqrt{\frac{\rho^2+6\alpha}{3\alpha^2}}\xi\right)}\right], \tag{34}$$

or

$$z(\xi)=\mp\sqrt{\frac{-A}{2\alpha B}}\left[\frac{\rho}{3}+\frac{\sqrt{\frac{\rho^2+6\alpha}{3}}\cot\left(\sqrt{\frac{\rho^2+6\alpha}{3\alpha^2}}\xi\right)}{1\pm\csc\left(\sqrt{\frac{\rho^2+6\alpha}{3\alpha^2}}\xi\right)}\right]. \tag{35}$$

Result 3. The authors have

$$A_0=\mp\frac{\rho}{3}\sqrt{\frac{-2}{\alpha}},\ A_1=\pm\sqrt{-\frac{3\alpha^3(1-\mu^2)}{2(\rho^2+6\alpha)}},\ B_1=\pm\sqrt{\frac{-2}{\alpha}},\ R=\frac{\rho^2+6\alpha}{3\alpha^2},\ \mu=\mu, \tag{36}$$
$$\delta=\mp\frac{\rho(2\rho^2+9\alpha)\sqrt{-2\alpha}}{27\alpha^2},$$

where $\alpha<0$, $\rho^2+6\alpha>0$ and $\alpha^3(1-\mu^2)<0$.

In this case, the authors deduce the exact wave solutions

$$z(\xi)=\pm\sqrt{\frac{-A}{2\alpha B}}\left[-\frac{\rho}{3}+\sqrt{\frac{\rho^2+6\alpha}{3}}\times\left(\frac{\left(\sqrt{1-\mu^2}\right)\sec\left(\sqrt{\frac{\rho^2+6\alpha}{3\alpha^2}}\xi\right)+\tan\left(\sqrt{\frac{\rho^2+6\alpha}{3\alpha^2}}\xi\right)}{\mu\sec\left(\sqrt{\frac{\rho^2+6\alpha}{3\alpha^2}}\xi\right)+1}\right)\right], \tag{37}$$

or

$$z(\xi)=\mp\sqrt{\frac{-A}{2\alpha B}}\left[\frac{\rho}{3}+\sqrt{\frac{\rho^2+6\alpha}{3}}\times\left(\frac{\left(\sqrt{1-\mu^2}\right)\csc\left(\sqrt{\frac{\rho^2+6\alpha}{3\alpha^2}}\xi\right)+\cot\left(\sqrt{\frac{\rho^2+6\alpha}{3\alpha^2}}\xi\right)}{\mu\csc\left(\sqrt{\frac{\rho^2+6\alpha}{3\alpha^2}}\xi\right)+1}\right)\right]. \tag{38}$$

Case 3. ($R=0,\mu=0$)

Substituting $\psi(\xi)=A_0+A_1\tau(\xi)$ into (17) and using (11), the left-hand side of Equation (17) becomes a polynomial in $\tau(\xi)$. Setting the coefficients of this polynomial to be zero, yields the following system of algebraic equations:

$$\tau^3(\xi):\quad A_1^3+2\alpha A_1=0,$$

$$\tau^2(\xi):\quad -\rho A_1+3A_0A_1^2=0,$$

$$\tau(\xi):\quad -A_1+3A_0^2A_1=0,$$

$$\tau^0(\xi):\quad A_0^3-A_0-\delta=0.$$

On solving the above, the algebraic equations using the Maple 14, the authors have the following result:

$$A_0=\pm\sqrt{\frac{1}{3}},\ A_1=\pm\rho\sqrt{\frac{1}{3}},\ \alpha=-\frac{1}{6}\rho^2,\ \delta=\mp\frac{2}{3}\sqrt{\frac{1}{3}}. \tag{39}$$

From (10), (16), (19) and (39), the authors deduce the following rational solution

$$z(\xi)=\pm\sqrt{\frac{A}{3B}}\left[1-\frac{\rho}{\xi}\right]. \tag{40}$$

Example 2. Exact solutions of the nonlinear PDE (2) describing the nonlinear dynamics of radial dislocations in MTs

In this subsection, the authors find the exact solutions of Equation (2). To this end, the authors use the transformation (4) to reduce Equation (2) into the following ODE:

$$\alpha\psi''(\xi)-\rho\psi'(\xi)+\psi(\xi)-\psi^3(\xi)=0, \tag{41}$$

where

$$\alpha = \frac{I\omega^2 - ch^2 k_1^2}{pH}, \rho = \frac{\omega\Gamma}{pH}, \quad (42)$$

and

$$\phi(\xi) = \sqrt{6}\psi(\xi). \quad (43)$$

Balancing $\psi''(\xi)$ with $\psi^3(\xi)$ in Equation (41), the authors get $N = 1$. Consequently, the authors have the formal solution of Equation (41) as follows:

$$\psi(\xi) = A_0 + A_1\sigma(\xi) + B_1\tau(\xi). \quad (44)$$

where A_0, A_1 and B_1 are constants to be determined later.

Substituting (44) into (41) and using (7) - (9), the left-hand side of Equation (41) becomes a polynomial in $\sigma(\xi)$ and $\tau(\xi)$. Setting the coefficients of this polynomial to be zero, yields the following system of algebraic equations:

$$\sigma^3(\xi): \quad -RA_1^3 - \varepsilon(\mu^2 + r)(2\alpha A_1\varepsilon^2 - 3A_1B_1^2) = 0,$$

$$\sigma^2(\xi): \quad -(\mu^2 + r)\varepsilon(-3A_0B_1^2 - \rho B_1\varepsilon) + 2\varepsilon R(2\alpha A_1\varepsilon^2 - 3A_1B_1^2)\mu - \varepsilon\alpha\mu RA_1 - 3RA_0A_1^2 = 0,$$

$$\sigma^2(\xi)\tau(\xi): \quad -3RA_1^2B_1 - \varepsilon(\mu^2 + r)(2\alpha B_1\varepsilon^2 - B_1^3) = 0,$$

$$\sigma(\xi): \quad -2\mu\varepsilon(3A_0B_1^2 + \rho B_1\varepsilon) - \varepsilon R(2\alpha A_1\varepsilon^2 - 3A_1B_1^2) + A_1 + \varepsilon\alpha A_1R - 3A_0^2A_1 + \rho\mu B_1 = 0,$$

$$\sigma(\xi)\tau(\xi): \quad -\varepsilon\rho A_1 - 6A_0A_1B_1 - 3\varepsilon\alpha\mu B_1 + 2\varepsilon\mu(2\alpha B_1\varepsilon^2 - B_1^3) = 0,$$

$$\tau(\xi): \quad 2\alpha B_1\varepsilon R + B_1 - 3A_0^2B_1 - \varepsilon R(2\alpha B_1\varepsilon^2 - B_1^3) = 0,$$

$$\sigma^0(\xi): \quad R\varepsilon(3A_0B_1^2 + \rho B_1\varepsilon) + A_0 - A_0^3 - \rho RB_1 = 0. \quad (45)$$

If the authors substitute $\varepsilon = -1$ into the algebraic Equations (45) and solve them by Maple 14, the authors have the following results:

Result 1. The authors have

$$A_0 = \pm\frac{1}{2},\ A_1 = 0,\ B_1 = \pm\frac{2}{3},\ R = \frac{9}{16\rho^2},\ \mu = 0, \alpha = \frac{2}{9}\rho^2, r = r. \quad (46)$$

From (12), (13), (43), (44) and (46), the authors deduce that if $r = -1$, then the authors have the exact wave solution

$$\phi(\xi) = \pm\frac{\sqrt{6}}{2}\left[1 + \tanh\left(\frac{3}{4\rho}\xi\right)\right], \quad (47)$$

while if $r = 1$, then the authors have the exact wave solution

$$\phi(\xi) = \pm\frac{\sqrt{6}}{2}\left[1 + \coth\left(\frac{3}{4\rho}\xi\right)\right]. \quad (48)$$

Note that our solution (47) is in agreement with the solution (43) obtained in Zdravkovic et al. (2014).

Result 2. The authors have

$$A_0 = \pm\frac{1}{2},\ A_1 = 0,\ B_1 = \pm\frac{1}{3}\rho,\ R = \frac{9}{4\rho^2},\ \mu = \pm\sqrt{-r}, \alpha = \frac{2}{9}\rho^2, \quad (49)$$

where $r < 0$.

In this case, the authors deduce that if $r = -1$, then the authors have the exact wave solution

$$\phi(\xi) = \pm\frac{\sqrt{6}}{2}\left[1 + \left(\frac{\tanh\left(\frac{3}{2\rho}\xi\right)}{1 \pm \operatorname{sech}\left(\frac{3}{2\rho}\xi\right)}\right)\right], \quad (50)$$

Result 3. The authors have

$$A_0 = \pm\frac{1}{2},\ A_1 = \pm\frac{2\rho^2\sqrt{r}}{9},\ B_1 = \pm\frac{1}{3}\rho,\ R = \frac{9}{4\rho^2},\ \mu = 0, \alpha = \frac{2}{9}\rho^2, \quad (51)$$

where $r > 0$.

In this case, the authors deduce that if $r = 1$, then the authors have the exact wave solution

$$\phi(\xi) = \pm\frac{\sqrt{6}}{2}\left[1 + \operatorname{csch}\left(\frac{3}{2\rho}\xi\right) + \coth\left(\frac{3}{2\rho}\xi\right)\right]. \quad (52)$$

Result 4. The authors have

$$A_0 = \pm\frac{1}{2},\ A_1 = \pm\frac{2\rho^2\sqrt{\mu^2 + r}}{9},\ B_1 = \pm\frac{1}{3}\rho,\ R = \frac{9}{4\rho^2},\ \mu = \mu, \alpha = \frac{2}{9}\rho^2, \quad (53)$$

where $\mu^2 + r > 0$.

In this case, the authors deduce that if $r = -1$, then the authors have the exact wave solution

$$\phi(\xi) = \pm\frac{\sqrt{6}}{2}\left[1 + \frac{\left(\sqrt{\mu^2 - 1}\right)\operatorname{sech}\left(\frac{3}{2\rho}\xi\right) + \tanh\left(\frac{3}{2\rho}\xi\right)}{\mu\operatorname{sech}\left(\frac{3}{2\rho}\xi\right) + 1}\right], \quad (54)$$

while if $r = 1$, then the authors have the exact wave

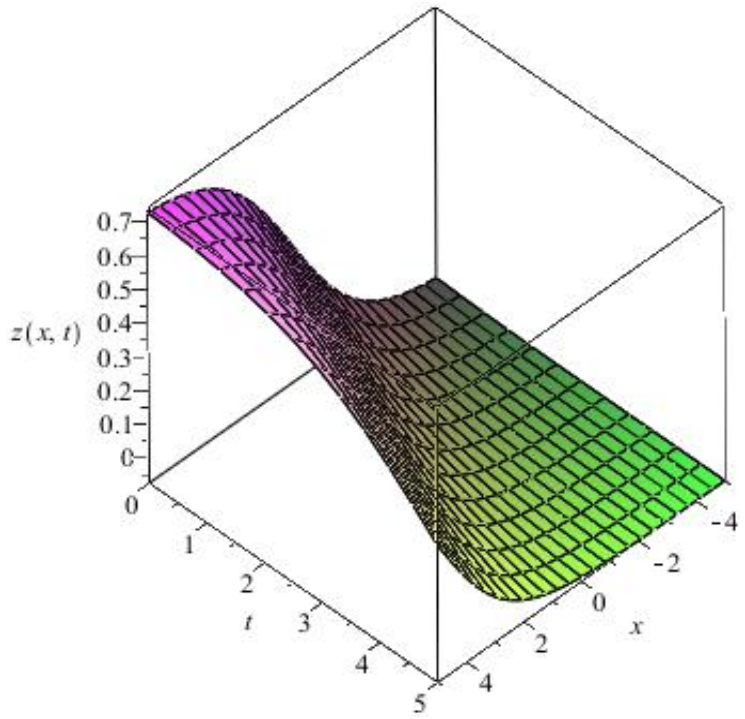

Figure 1. The plot of (23) when $k_1 = 1, \omega = 1, \alpha = -1, \rho = 2, A = 1, B = 2.$

$$\phi(\xi) = \pm\frac{\sqrt{6}}{2}\left[1 + \frac{\left(\sqrt{\mu^2+1}\right)\operatorname{csch}\left(\frac{3}{2\rho}\xi\right) + \coth\left(\frac{3}{2\rho}\xi\right)}{\mu\operatorname{csch}\left(\frac{3}{2\rho}\xi\right)+1}\right]. \qquad (55)$$

solution. Finally, note that the case $\varepsilon = 1, r = -1, R > 0,$ is rejected for example 2, because the authors have complex solutions for Equation (2).

PHYSICAL EXPLANATIONS OF SOME OBTAINED SOLUTIONS

Solitary waves can be obtained from each traveling wave solution by setting particular values to its unknown parameters. In this section, the authors have presented some graphs of solitary waves constructed by taking suitable values of involved unknown parameters to visualize the underlying mechanism of the original equation. Using mathematical software Maple 14, three dimensional plots of some obtained exact traveling wave solutions have been shown in Figures 1 to 6.

The nonlinear PDE (1) describing the nonlinear dynamics of MTs as nanobioelectronics transmission lines

The obtained solutions for the nonlinear PDE (1) incorporate three types of explicit solutions namely, hyperbolic, trigonometric and rational. From these explicit results, it is easy to say that the solution (23) is a kink shaped soliton solution; the solution (24) is a singular kink shaped soliton solution; the solutions (26), (28) are bell-kink shaped soliton solution; the solution (29) is a singular bell-kink shaped soliton solution, the solutions (31), (32), (34), (35), (37), (38) are periodic solutions and the solution (40) is rational solution. The graphical representation of the solutions (23), (26), (34) and (38) can be plotted as shown in Figures 1 to 4.

The nonlinear PDE (2) describing the nonlinear dynamics of radial dislocations in MTs

The obtained solutions for the nonlinear PDE (2) are hyperbolic. From the obtained solutions for this equation, the authors observe that the solution (47) is a kink shaped soliton solution, the solution (48) is a singular kink shaped soliton solution, the solution (50), (54) are bell-kink shaped soliton solutions and the solutions (52), (55) are singular bell-kink shaped soliton solutions. The graphical representation of the solutions (52) and (54) can be plotted as shown in Figure 5 and 6.

Remark: The authors have checked all our solutions with Maple 14 by putting them back into the original Equations (1) and (2).

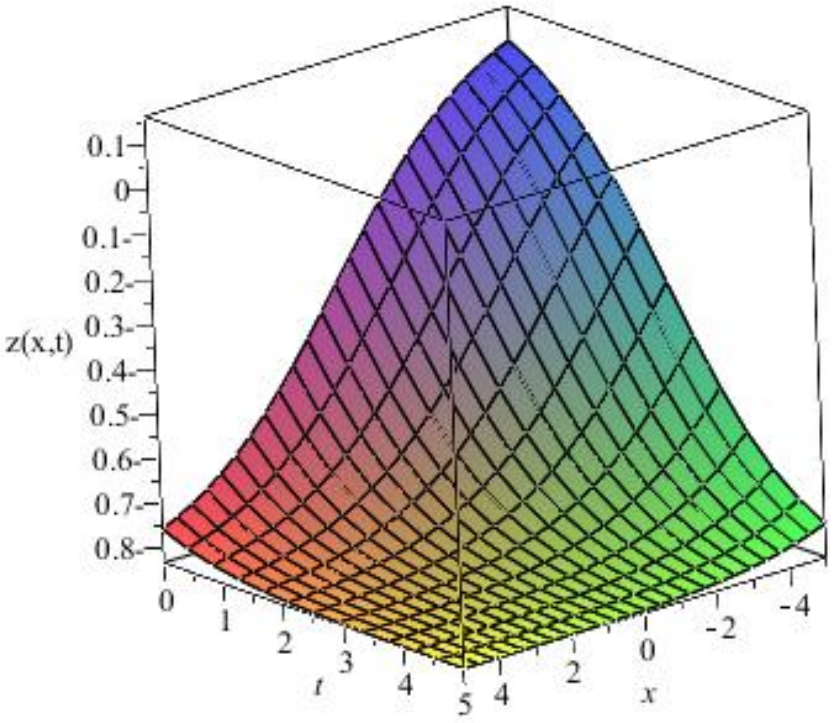

Figure 2. The plot of (26) when $k_1 = 1, \omega = -2, \alpha = -2, \rho = 2, A = 1, B = 1.$

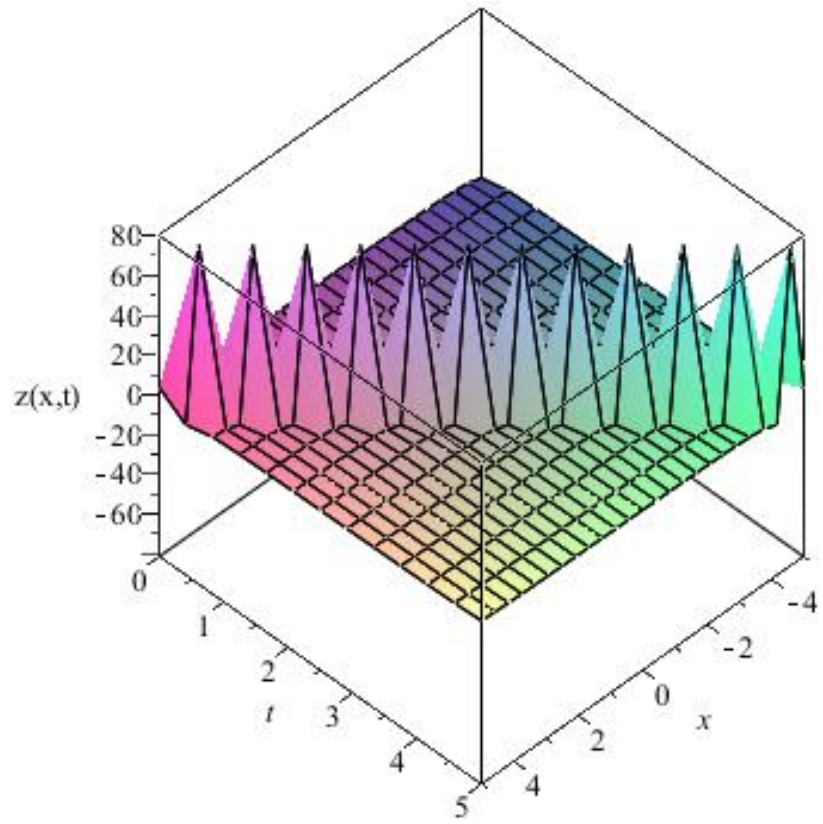

Figure 3. The plot of (34) when $k_1 = 1, \omega = -1, \alpha = -2, \rho = 4, A = 1, B = 1.$

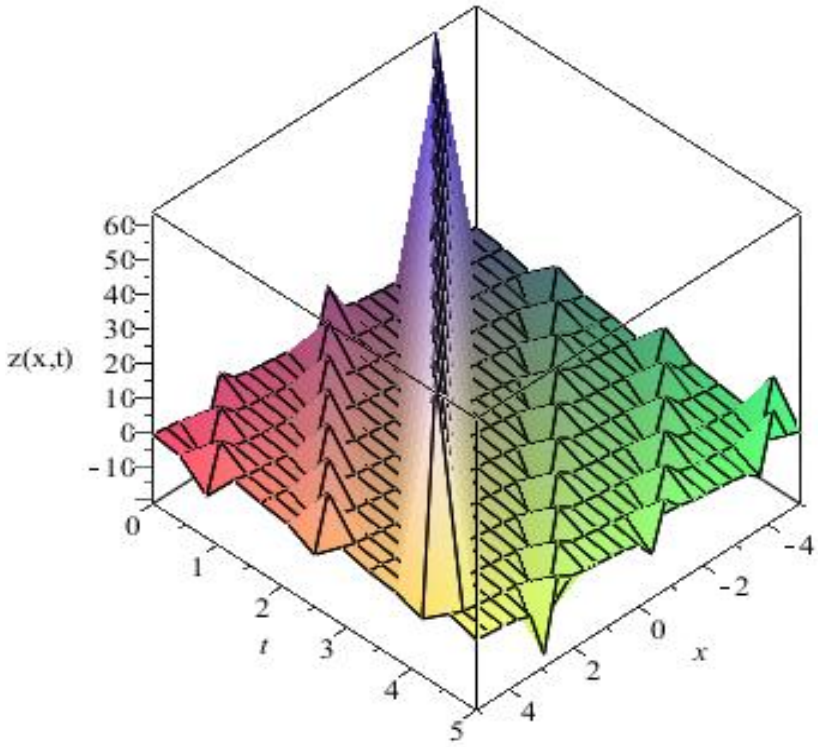

Figure 4. The plot of (38) when $k_1 = 1, \omega = 2, \alpha = -1, \rho = 4, A = 1, B = 1, \mu = \frac{1}{2}$.

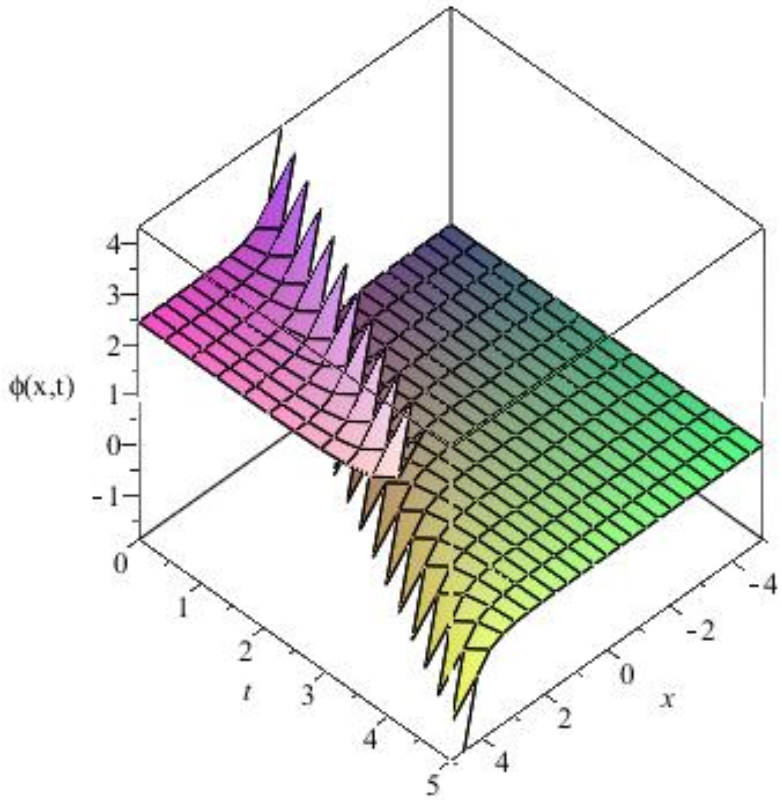

Figure 5. The plot of (52) when $k_1 = 2, \omega = 2, \rho = \frac{3}{2}$.

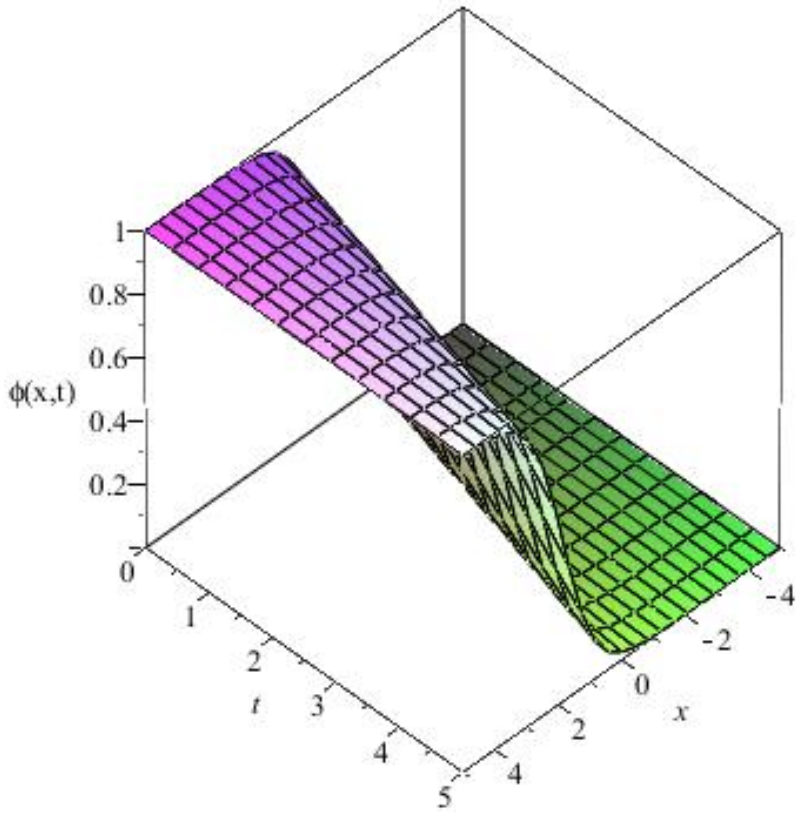

Figure 6. The plot of (54) when $k_1 = 2, \omega = 1, \rho = \frac{3}{2}, \mu = 2.$

Conclusions

The generalized projective Riccati equations method was used in this paper to obtain some new exact solutions of the two nonlinear evolution Equations (1) and (2) which describe the model of MTs as nano-bioelectronics transmission lines and the dynamics of radial dislocations in MTs, respectively. On comparing our results in this paper with the well-known results obtained in Zekovic et al. (2014) and Zdravkovic et al. (2014), the authors deduce that their results are new and not published elsewhere except the result (47) which is in agreement with the result of (43) obtained in Zdravkovic et al. (2014). It is to be noted here that the obtained solutions are of type kink, soliton with singularities and periodic. Solitons are the solutions in the form $\sec h$ and $\sec h^2$, the graph of soliton is a wave that goes up only. It is not like periodic solutions sine, cosine, etc, as in trigonometric function, that goes above and below the horizontal. Kink is also called a soliton; it is in the form $\tanh$ not $\tanh^2$. In kink the limit as $x \to \infty$, the answer is a constant, not like solitons where the limit goes to 0 (Alquran and Al-Khaled, 2011a, b, 2012; Alquran, 2012; Shukri and Al-khaled, 2010; Alquran et al., 2012; Alquran and Qawasmeh, 2014).

Conflict of Interest

The authors declare no conflict of interests.

ACKNOWLEDGEMENT

The authors wish to thank the referees for their comments.

REFERENCES

Abdou MA (2007). The extended F-expansion method and its application for a class of nonlinear evolution equations. Chaos Solitons Fractals 31:95–104.

Alam MN, Akbar MA (2013). Exact traveling wave solutions of the KP-BBM equation by using the new approach of generalized $(\frac{G'}{G})$-expansion method. Springer Plus. 2:617. DOI: 10.1186/2193-1801-2-617.

Alam MN, Akbar MA (2014a). Traveling wave solutions for the mKdV equation and the Gardner equation by new approach of the generalized $(\frac{G'}{G})$-expansion method. J. Egyptian Math. Soc. 22:402-406.

Alam MN, Akbar MA (2014b). Application of the new approach of generalized $(\frac{G'}{G})$-expansion method to find exact solutions of nonlinear PDEs in mathematical physics. BIBECHANA. 10:58-70.

Alam MN, Akbar MA, Fetama K, Hatez MG (2014a). Exact traveling wave solutions of the (2+1)-dimensional modified Zakharov-Kuznetsov equation via new extended $\left(\frac{G'}{G}\right)$-expansion method. Elixir Appl. Math. 73:26267-26276.

Alam MN, Akbar MA, Hoque MF (2014b). Exact traveling wave solutions of the (3+1)-dimensional mKdV-ZK equation and the (1+1)-dimensional compound KdVB equation using new approach of the generalized $\left(\frac{G'}{G}\right)$-expansion method. Pramana J. Phys. 83:317-329.

Alam MN, Akbar MA, Mohyud-Din ST (2014c). A novel $\left(\frac{G'}{G}\right)$-expansion method and its application to the Boussinesq equation. Chin. Phys. B. 23:020203-020210.

Alam MN, Akbar MA, Mohyud-Din ST (2014d). General traveling wave solutions of the strain wave equation in microstructured solids via the new approach of generalized $\left(\frac{G'}{G}\right)$-Expansion method. Alexandria Eng. J. 53:233–241.

Alam MN, Akbar MA (2015). Some new exact traveling wave solutions to the simplified MCH equation and the (1+1)-dimensional combined KdV-mKdV equations. J. Assoc. Arab Univ. Basic Appl. Sci. 17:6–13.

Alquran M, Al-Khaled K (2011a). The tanh and sine-cosine methods for higher order equations of Korteweg-de Vries type. Physica Scripta. 84:025010.

Alquran M, Al-Khaled K (2011b). Sinc and solitary wave solutions to the generalized Benjamin-Bona-Mahony- Burgers equations. Physica Scripta. 83: 065010.

Alquran M (2012). Solitons and periodic solutions to nonlinear partial differential equations by the Sine- Cosine method. Appl. Math. Inf. Sci. 6:85-88.

Alquran M, Al-khaled K (2012). Mathematical methods for a reliable treatment of the (2+1)-dimensional Zoomeron equation. Math. Sci. 6:12 doi:10.1186/2251-7456-6-11.

Alquran M, Ali M, Al-Khaled K (2012). Solitary wave solutions to shallow water waves arising in fluid dynamics. Nonlinear Studies. 19:555-562.

Alquran M, Qawasmeh A (2014). Soliton solutions of shallow water wave equations by means of $\left(\frac{G'}{G}\right)$-expansion method. J. Appl. Anal. Comput. 3:221-229.

Aminikhad H, Moosaei H, Hajipour M (2009). Exact solutions for nonlinear partial differential equations via Exp-function method. Numer. Methods Partial Differ. Equ. 261427–1433.

Bekir A, Unsal O (2012). Analytic treatment of nonlinear evolution equations using the first integral method. Pramana J. Phys. 79:3-17.

Bountis TC, Papageorgiou V, Winternitz P (1986). On the integrability of systems of nonlinear ordinary differential equations with superposition principles. J. Math. Phys. 27:1215-1224.

Conte R, Musette M (1992). Link between solitary waves and projective Riccati equations. Phys. A: Math. Cen. 25:2609-2623.

Dai CQ, Zhang JF (2006). Jacobian elliptic function method for nonlinear differential- difference equations. Chaos Solitons Fractals. 27:1042–1049.

EL-Wakil SA, Abdou MA (2007). New exact traveling wave solutions using modified extended tanh-function method. Chaos Solitons Fractals 31:840–852.

Fan E, Zhang H (1998). A note on the homogeneous balance method. Phys. Lett. A. 246: 403–406.

Fan E (2000). Extended tanh-function method and its applications to nonlinear equations. Phys. Lett. A. 277:212–218.

Fan E, Zhang J (2002). Applications of the Jacobi elliptic function method to special type nonlinear equations, Phys. Lett. A. 305:383–392.

Feng ZS (2002). The first integral method to study the Burgers–KdV equation. J. Phys. A: Math. Gen. 35:343–349.

Hafez MG, Alam MN, Akbar MA (2014). Traveling wave solutions for some important coupled nonlinear physical models via the coupled Higgs equation and the Maccari system. J. King Saud Univ. Sci. doi: http://dx.doi.org/10.1016/j.jksus.2014.09.001.

Hayek M (2010). Constructing of exact solutions to the KdV and Burgers equations with power law nonlinearity by the extended $\left(\frac{G'}{G}\right)$-expansion method. Appl. Math. Comput. 217: 212–221.

He JH, Wu XH (2006). Exp-function method for nonlinear wave equations. Chaos Solitons Fractals 30:700–708.

Jawad AJM, Petkovic MD, Biswas A (2010). Modified simple equation method for nonlinear evolution equations. Appl. Math. Comput. 217:869–877.

Liu S, Fu Z, Liu S, Zhao Q (2001). Jacobi elliptic function expansion method and periodic wave solutions of nonlinear wave equations. Phys. Lett. A. 289:69–74.

Lu BHQ, Zhang HQ, Xie FD (2010). Traveling wave solutions of nonlinear partial differential equations by using the first integral method. Appl. Math. Comput. 216:1329-1336.

Ma WX, Wu HY, He JS (2007). Partial differential equations possessing Frobenius integrable decomposition technique. Phys. Lett. A. 364:29-32.

Ma WX, Lee JH (2009). A transformed rational function method and exact solutions to the (3+1) dimensional Jimbo-Miwa equation. Chaos, Solitons Fractals 42:1356-1363.

Ma WX, Huang T, Zhang Y (2010). A multiple exp-function method for nonlinear differential equations and its application. Phys. Script. 82:065003.

Ma WX, Zhu Z (2012). Solving the (3+1)-dimensional generalized KP and BKP equations by the multiple exp-function algorithm. Appl. Math. Comput. 218:11871-11879.

Malfiieiet W (1992). Solitary wave solutions of nonlinear wave equation. Am. J. Phys. 60: 650–654.

Malfiieiet W, Hereman W (1996). The tanh method: Exact solutions of nonlinear evolution and wave equations. Phys. Scr. 54:563–568.

Moosaei H, Mirzazadeh M Yildirim A (2011). Exact solutions to the perturbed nonlinear Schrodinger equation with Kerr law nonlinearity by using the first integral method. Nonlinear Anal.: Model. Control. 16:332–339.

Ren YJ, Zhang HQ (2006). A generalized F-expansion method to find abundant families of Jacobi elliptic function solutions of the (2+1)-dimensional Nizhnik-Novikov-Veselov equation. Chaos Solitons Fractals. 27:959–979.

Shukri S, Al-khaled K (2010). The extended tanh method for solving systems of nonlinear wave equations. Appl. Math. Comput. 217:1997-2006.

Wang ML (1996). Exact solutions for a compound KdV-Burgers equation. Phys. Lett. A. 213:279–287.

Wazwaz AM (2004a). The tanh method for travelling wave solutions of nonlinear equations. Appl. Math. Comput. 154:714–723.

Wazwaz AM (2004b). A sine-cosine method for handling nonlinear wave equations. Math. Comput. Model. 40:499–508.

Wazwaz AM (2005). Exact solutions to the double sinh-Gordon equation by the tanh method and a variable separated ODE Method. Comput. Math. Appl. 50:1685–1696.

Wazwaz AM (2007). The extended tanh method for abundant solitary wave solutions of nonlinear wave equations. Appl. Math. Comput. 187:1131–1142.

Yan C (1996). A simple transformation for nonlinear waves. Phys. Lett. A. 224:77-84.

Yang AM, Yang X J, Li ZB (2013). Local fractional series expansion method for solving wave and diffusion equations on cantor sets. Abst. Appl. Anal. Article ID 351057: P.5.

Yang YJ, Baleanu D, Yang XJ (2013). A Local fractional variational iteration method for Laplace equation within local fractional operators. Abst. Appl. Anal. Article ID 202650:P.6.

Yan ZY (2003). Generalized method and its application in the higher-order nonlinear Schrodinger equation in nonlinear optical fibres. Chaos, Solitons Fractals 16:759-766.

Yomba E (2005). The general projective Riccati equations method and exact solutions for a class of nonlinear partial differential equations. Chin. J. Phys. 43:991-1003.

Younis M (2014a). Soliton solutions of fractional order KdV-Burger's equation. J. Adv. Phys. 4:325-328.

Younis M (2014b). New exact travelling wave solutions for a class of nonlinear PDEs of fractional order. Math. Sci. Lett. 3:193-197.

Younis M, Zafar A (2014). Exact solution to nonlinear differential equations of fractional order via $\left(\frac{G'}{G}\right)$-expansion method. Appl. Math. 5:1-6.

Zayed EME (2009). The $\left(\frac{G'}{G}\right)$-expansion method and its applications to some nonlinear evolution equations in mathematical physics. J. Appl. Math. Comput. 30:89–103.

Zayed EME, Gepreel KA (2009). The $\left(\frac{G'}{G}\right)$-expansion method for finding traveling wave solutions of nonlinear partial differential equations in mathematical physics. J. Math. Phys. 50:013502–013513.

Zayed EME (2011). A note on the modified simple equation method applied to Sharma- Tasso- Olver equation. Appl. Math. Comput. 218:3962–3964.

Zayed EME, Hoda Ibrahim SA (2012). Exact solutions of nonlinear evolution equation in mathematical physics using the modified simple equation method. Chin. Phys. Lett. 29:060201–4.

Zayed EME, Arnous AH (2012). Exact solutions of the nonlinear ZK-MEW and the potential YTSF equations using the modified simple equation method. AIP Conf. Proc. 1479:2044–2048.

Zayed EME, Hoda Ibrahim SA (2013a). The two variable $\left(\frac{G'}{G},\frac{1}{G}\right)$-expansion method for finding exact traveling wave solutions of the (3+1) -dimensional nonlinear Potential Yu-Toda-Sasa-Fukuyama equation. Int. Conf. Adv. Comput. Sci. Electronics Inf. Atlantis Press, pp. 388-392.

Zayed EME, Hoda Ibrahim SA (2013b). Modified simple equation method and its applications for some nonlinear evolution equations in mathematical physics. Int. J. Comput. Appl. 67:39–44.

Zayed EME, Alurrfi KAE (2014a). The $\left(\frac{G'}{G},\frac{1}{G}\right)$-expansion method and its applications to find the exact solutions of nonlinear PDEs for nanobiosciences. Math. Prob. Eng. Article ID 521712: P.10.

Zayed EME, Alurrfi KAE (2014b). The $\left(\frac{G'}{G},\frac{1}{G}\right)$-expansion method and its applications for solving two higher order nonlinear evolution equations. Math. Prob. Eng. Article ID 746538: P.21.

Zayed EME, Alurrfi KAE (2014c). On solving the nonlinear Schrödinger-Boussinesq equation and the hyperbolic Schrödinger equation by using the $\left(\frac{G'}{G},\frac{1}{G}\right)$-expansion method. Int. J. Phys. Sci. 19:415-429.

Zayed EME, Alurrfi KAE (2014d). The generalized projective Riccati equations method for solving nonlinear evolution equations in mathematical physics. Abst. Appl. Anal. Article ID 259190: P.10.

Zayed EME, Hoda Ibrahim SA (2014). Exact solutions of Kolmogorov-Petrovskii- Piskunov equation using the modified simple equation method. Acta Math. Appl. Sinica. English series. 30:749-754.

Zdravkovic S, Sataric MV, Maluckov A, Balaz A (2014). A nonlinear model of the dynamics of radial dislocations in microtubules. Appl. Math. Comput. 237:227-237.

Zekovic S, Muniyappan A, Zdravkovic S, Kavitha L (2014). Employment of Jacobian elliptic functions for solving problems in nonlinear dynamics of microtubules. Chin. Phys. B. 23:020504.

Zhang GX, Duan YS, Li ZB (2001). Exact solitary wave solutions of nonlinear wave equations. Science China A. 44:396-401.

Zhang JL, Wang ML, Wang YM, Fang ZD (2006). The improved F-expansion method and its applications. Phys. Lett. A. 350:103–109.

Zhang S, Tong JL, Wang W (2008). A generalized $\left(\frac{G'}{G}\right)$-expansion method for the mKdv equation with variable coefficients. Phys. Lett. A. 372:2254–2257.

Zhang ZY (2008). New exact traveling wave solutions for the nonlinear Klein-Gordon equation. Turk. J. Phys. 32:235-240.

Zhao XQ, Zhi HY, Zhang HQ (2006). Improved Jacobi elliptic function method with symbolic computation to construct new double-periodic solutions for the generalized Ito system. Chaos Solitons Fractals. 28:112–126.

academicJournals

Vol. 10(13), pp. 403-412, 16 July, 2015
DOI: 10.5897/IJPS2015.4360
Article Number: 695003A54075
ISSN 1992 - 1950

http://www.academicjournals.org/IJPS

International Journal of Physical Sciences

Full Length Research Paper

Nanocrystalline Cadmium sulfide (CdS) thin film synthesized at different dip times by chemical bath deposition technique

B. A. Ezekoye[1]*, K. O. Ighodalo[1], V. A. Ezekoye[1], T. M. Emeakaroha[1], J. I. Ezema[1] and P. O. Offor[2]

[1]Department of Physics and Astronomy, University of Nigeria.
[2]Department of Metallurgical and Materials Engineering, University of Nigeria.

Received 29 April, 2015; Accepted 26 June, 2015

Nanocrystalline Cadmium sulfide (CdS) thin films were prepared by chemical bath deposition technique on a glass substrates at a temperature of 80°C and at different deposition times with composition of cadmium chloride ($CdCl_2$), thiourea ($CS(NH_2)_2$), ammonia solution (NH_4OH) and triethanolamine (TEA) solution. The characterization of thin films was carried out for the structural, morphological and optical properties using X-ray diffraction (XRD), Scanning electron microscope (SEM) and UV-VIS spectrophotometer. XRD studies show that the preferential orientation (002), analysis shows that the prepared samples have hexagonal crystal structure. Scanning electron microscopy (SEM) reveals small nanosized grains tied up in a fibrous-like porous structure uniformly distributed over the surface of the substrate for the CdS films. A UV-VIS optical spectroscopy study was carried out to determine the band gap of the nanocrystalline CdS thin films. The average band gap was found to be 2.25 eV, which is lower than the bulk value (2.4 eV). The increase in absorption coefficient with photon energy makes the deposited CdS thin film a suitable candidate for the fabrication of solar cells.

Key words: Nanocrystalline Cadmium sulfide (CdS), X-Ray diffraction, scanning electron microscopy, solar energy.

INTRODUCTION

The conversion of sunlight directly into electricity using the electronic properties of suitable materials appears to be an elegant energy conversion process and an ideal alternative to conventional energy sources. It has being a research laboratory interest for more than a hundred years, the solar cell technology has seen enormous development during the last four decades, initially for providing electrical power for space crafts and more recently for terrestrial applications (Mathew, 2009). Among the II-VI semiconductors, CdS polycrystalline thin films is a representative material with a wide energy gap semiconductors. This CdS thin film has experienced a fast rising mainly due to its applications in piezoelectric transducers, laser materials and photovoltaic cells, also it can be used as a window material together with several semiconductors such as CdTe, Cu_2S and $CuInSe_2$

*Corresponding author. E-mail: benjamin.ezekoye@unn.edu.ng

(Selma et al., 2009; Mahdi et al., 2009). In CdS/CdTe heterojunction solar cells, where CdS acts as the n-type semiconductor for the window layer, a thicker CdS layer is believed to yield lower transmittance. In addition, as CdS films become thinner, the probability of a short circuit between the CdTe and the front contact increases. In order to prepare transparent and high resistivity CdS thin films with the good conformal coverage (Maeng et al., 2011). Ximello-Quiebras et al. (2004), deposited CdS with time variation at constant temperature from an aqueous ammoniacal solution containing cadmium ion from cadmium chloride and thiourea reported hexagonal phase with a preferential (0 0 2) orientation, dark resistivity of 10^4 Ωcm and with band gap in the range of 2.4eV. (Demir and Gode, 2015) obtained a band gap between 2.15-2.25eV with electrical conductivity of the films calculated from the current–voltage characteristic in the dark increases from 5.482×10^{-10} $(\Omega\ cm)^{-1}$ to 5.304×10^{-8} $(\Omega\ cm)^{-1}$. The CBD process, adapted for the preparation of CdS window layers in high efficiency solar cells, includes a cadmium salt, a complexing agent, and thiourea as Sulphur source, these precursors are mixed in an alkaline aqueous solution (Liu et al., 2010). Various deposition techniques such as electrodeposition (Bastol et al., 1985), spray pyrolysis (Chamberlain and Skarman, 1966), successive ionic layer adsorption reaction (Partha and Ayan, 2014) and a new chemical bath technique under rotation (Oliva-Avilés et al., 2010). Among these various techniques, the CBD is the most successful method used in the production of uniform, adherent, and reproducible large-area thin films for solar related application (Mane and Lokhande, 2000; Ximello-Quiebras et al., 2006). Thus, the deposition rate can be modified not only by changing the chemical reagents concentrations, or with the type of bath agitation used during deposition or by changing the bath temperature, it can also be modified by deposition time. The importance of this deposition changes can determine the thickness of the film and the bath and or substrate agitation can be directly related with the physical properties of the CdS films (Moualkia et al., 2009). In this research, the authors report a systemic investigation on the effect of deposition time on the physical properties of CBD–CdS films such as structure, surface morphology and properties using X-ray diffraction (XRD), scanning electron microscopy (SEM) and optical transmission (UV).

EXPERIMENTAL DETAILS

Chemical reaction

The growth of CdS by CBD is given by the decomposition of the thiourea $(NH_2)_2SC$ in presence of a cadmium salt ($(CdCl_2.2\frac{1}{2}H_2O)$) in a basic solution with ammonia (NH_3) as complexing agent. The chemical process can be described through the following chemical reactions:

$$Cd(NH_3)_4^{2+} \rightarrow 4NH_3 + Cd^{2+} \quad (1)$$

$$NH_3 + H_2O \rightarrow NH_4 + OH^- \quad (2)$$

$$Cd(NH_2)_2 + OH^- \rightarrow SH^- + CH_2N_2 + H_2O \quad (3)$$

$$SH^- + OH^- \rightarrow +H_2O \quad (4)$$

$$Cd^{2+} + S^{2-} \rightarrow CdS \quad (5)$$

Synthesis

Thin films were deposited on glass substrate (micro slide - 75 mm L × 25 mm wide), thickness 1.45 mm (±0.1 mm). The glass substrates were first washed with detergent and rinsed thoroughly with normal water 2-3 times, subsequently soaking them in acetone for 45 min. After that the slides were thoroughly washed by deionized water several times, ultrasonicated in an ultrasonicator for 10 min. and dried in an oven at 60°C for 15 min. The chemical bath solution was prepared by 0.2 molar solution of cadmium chloride ($CdCl_2.2\frac{1}{2}H_2O$) as the Cd^{2+} ion source, 0.1 molar solution of thiourea $(NH_2)_2SC$ as the S^{2-} ion source, 30% ammonium (NH_3) and triethanolamine (TEA) $(N(CH_2CH_2OH)_3)$. 10 ml of cadmium chloride was complexed with 5 ml of TEA in a 100 mls capacity of beaker, then 5 ml of ammonium solution was added to the 100 ml capacity beaker making the solution colourless, then 10 ml of thiourea was added to the already solution. The mixture was then topped to 80 ml level by addition of 40 ml of distilled water and stirred gently to ensure uniform mixture. The glass substrate was dipped vertically suspended into beaker containing the solution. The optimal deposition temperature and dip time for cadmium sulphide thin films was 80±2°C during the growth and 40, 60 and 80 min, respectively, during which the solution color changed to dip yellow as the deposition time increases. At the end of the deposition CdS thin film formed on the substrates with desired thickness, adherent, homogeneous and yellowish without any powder precipitation. The substrates were removed from the chemical bath, rinsed thoroughly in distilled water and dried in the air at room temperature.

Characterization techniques

The films were structurally characterized by X-ray diffraction (XRD). X-ray diffractometer in the range of scanning angle (20° - 120°) with CuK_α radiation (45 Kv, 40 mÅ) of wavelength λ = 1.54443Å. Optical properties of Cadmium sulfide films with UV-VIS spectrophotometer to measure the absorbance of the films in the range of wavelengths 400 – 1100 nm. For the morphological properties of the thin film, the authors used the Scanning Electron Microscope (SEM) at X1000 magnification and scale bar length of 100 µm. Finally, Energy Dispersive X ray (EDAX) is used to determine the quantitative composition on the deposited thin film on the glass substrate with count up to 1000 with electron volts of range 0 – 20.

RESULTS AND DISCUSSION

Structural characteristics of the films

CdS films, which were deposited on glass, can have either a hexagonal or a cubic structure or a mixed

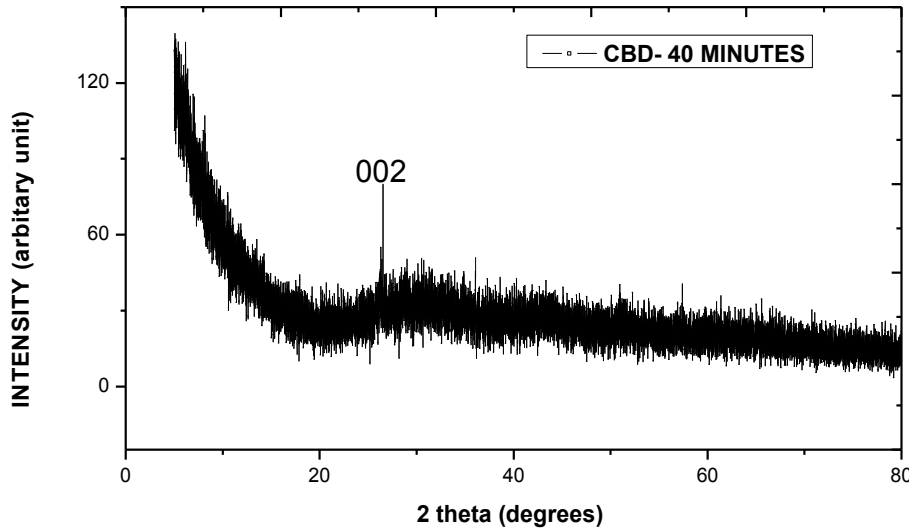

Figure 1. XRD pattern of CdS thin film – 40 min.

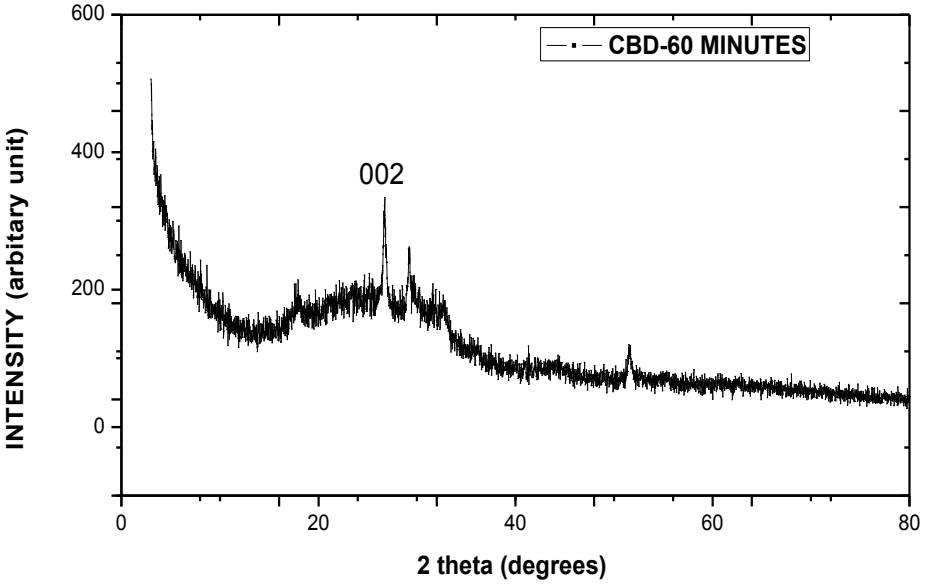

Figure 2. XRD pattern of CdS thin film – 60 min.

structure of the two, depending on the condition in which the film is prepared (Enriquez and Mathew, 2003). The structural analysis of CdS thin film was carried out by using X-ray diffractometer in the range of scanning angle (20° - 120°). Figures 1, 2 and 3 shows X ray diffraction patterns of CdS film deposited at different time interval at 80°C. The CdS films was found to be hexagonal crystal structure with strong orientation associated with (0 0 2) reflection according to data file reference no.01-074-9664. For the XRD pattern of CdS film at 40, 60 and 80 min all showed prominent peaks at 2θ = 26.25°, 26.67°, 26.76°, which corresponds to the (002) lattice plane. The results of X-ray analysis are agreed with earlier investigators report (Gopinathan et al., 2011; Kodigala et al., 2001; Fangyang et al., 2010). The crystalline size of the deposited film is calculated using FWHM data and Debye-Scherer formula, $D = k\lambda/\beta\cos\theta$, where k is a Scherer's constant taken to be 0.94, λ the wavelength of X-ray used (λ = 1.54443Á), D = Grain Size, θ = is Bragg's diffraction angle at peak position and β = is Full width at half maximum of the peak in radian. Using Scherer's formula grain or particle size was found to be of the order range between 11 to 15 nm.

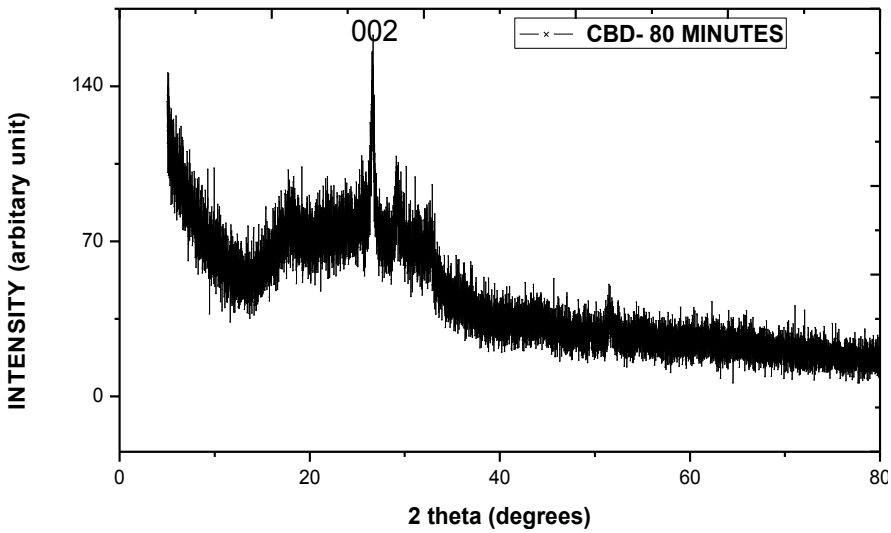

Figure 3. XRD pattern of CdS thin film – 80 min.

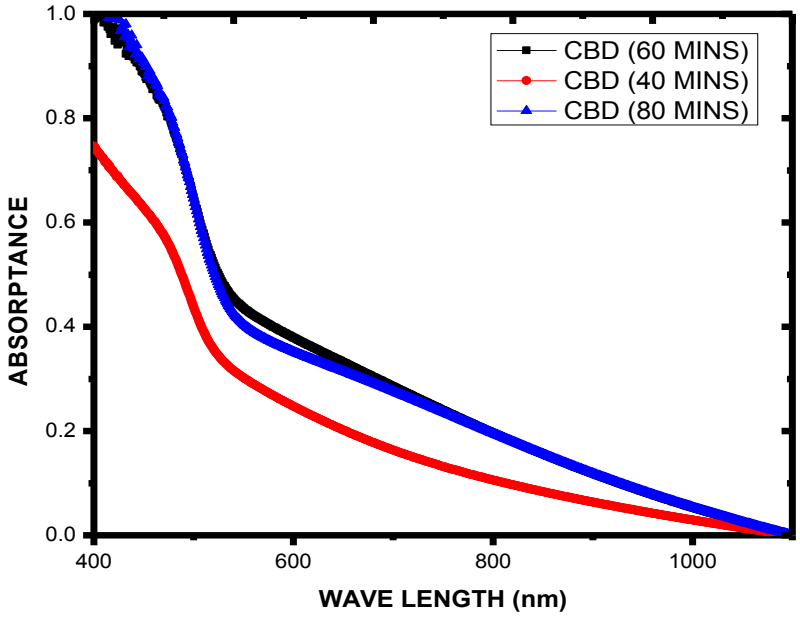

Figure 4. Absorbance spectra of CBD-CdS film at 40, 60 and 80 min.

Optical properties of CdS thin films

Figure 4 shows the absorption spectra of the deposited CBD-CdS of different samples at 40, 60, and (80 min), respectively. The figure shows a high absorbance in the visible region between (400 to 520 nm) and a corresponding decrease in absorbance as the wavelength increases along the near infra-red region. The decrease in absorbance in the near infra-red region shows high transmittance near the infra-red region of the spectrum (Ezema et al., 2010) for all samples of CdS and low transmittance in the visible light region for all samples. Figure 5 shows the reflectance spectra of the deposited CBD-CdS of different samples at 40, 60, and (80 min), respectively. The figures shows a high reflectance in the wavelength range of visible light region (400 – 490) nm and a gradual fall in the reflectance in the wavelength range of 500 – 1100 nm was observed for all samples deposited by chemical bath deposition.

Figure 6 shows the variations of absorption coefficient (α) with photon energy for CdS thin films for all deposited samples CBD-CdS thin film of different samples at 40,

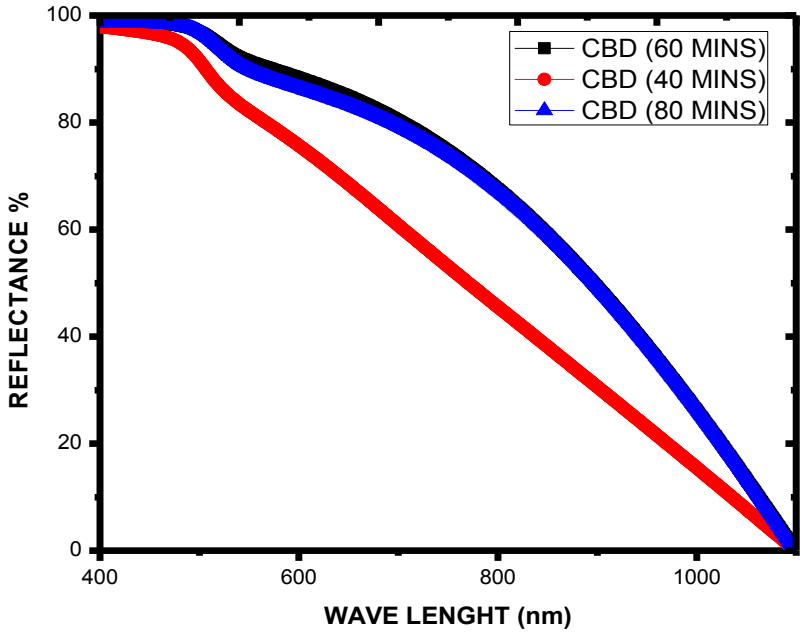

Figure 5. Reflectance spectra of CBD-CdS film at 40, 60 and 80 min.

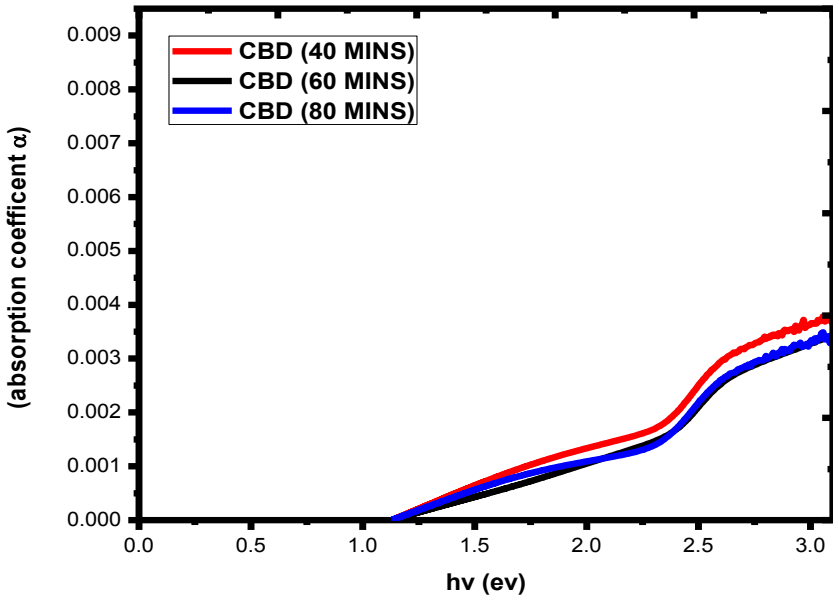

Figure 6. Plot of the variation of absorption coefficient (α) with photon energy (eV) of CBD-CdS at 40, 60 and 80 min.

60, and (80 min), respectively, the result reveals that there is a gradual increase in the absorption coefficient with increase photon energy for all the samples (Awodugba et al., 2012; Awodugba and Adedokun, 2011). As the photon energy increases, not just the electrons already having energy close to that of the band gap can interact with the photon. Therefore, a larger number of electrons can interact with the photon and result in the photon being absorbed. Materials with higher absorption coefficients more readily absorb photons, which excite electrons into the conduction band. This increase in absorption coefficient of the deposited CdS thin film makes it suitable in the designing of solar cells.

The absorption coefficient α associated with the strong

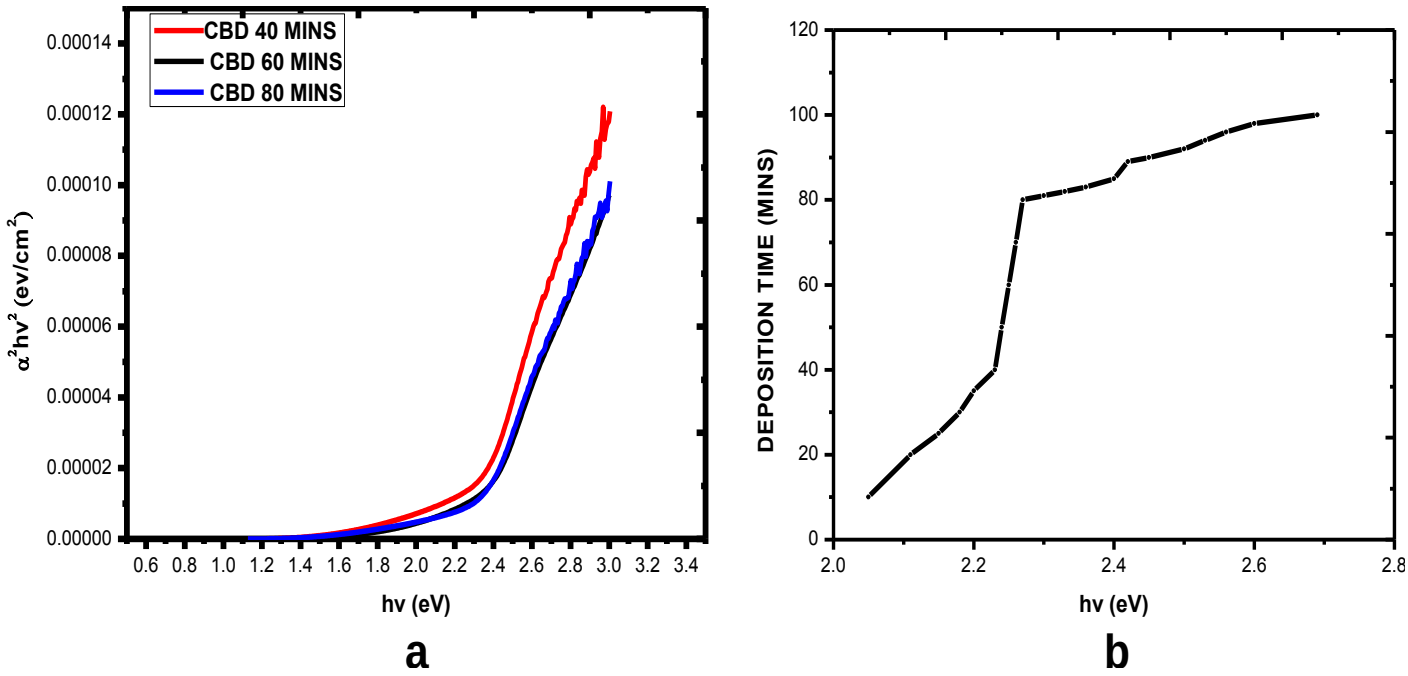

Figure 7. a) Plot of Photon energy (eV) dependence on α^2hv^2 eV/cm^2 CBD-CdS at 40, 60 and 80 min; b) Plot of photon energy (eV) dependence on deposition time (mins).

absorption region of the film was calculated from absorbance (A) and the thin film thickness (t) using the relation (Jadhav et al., 2014; Fajinmi and Adelabu, 2009):

$$\alpha = 2.3026\,A/t \quad (6)$$

In semiconductors, the relation connecting the absorption coefficient α, the incident photon energy (hv) and optical band gap E_g takes the form (Ezema et al., 2010):

$$(\alpha hv) = K(hv - E_g)^{n/2} \quad (7)$$

where K is a constant, E_g is separation between valence and conduction bands and n is equal to 1 which makes it ½ for direct band gap semiconductor, also 2, 3/2 or 3 correspond to indirect, forbidden direct or forbidden indirect transitions, respectively. CdS as a semiconductor material has received much attention due to its direct band gap resulting in emission in the visible wavelength (Abdullah et al., 2012). The band gap of the films was determined by plotting a graph between $(\alpha hv)^2$ and (hv). The band gap energy (Eg) was estimated by a linear interpolation of each curve to energy axis. Figure 7a shows optical energy band gaps of the CBD-CdS thin film for 40, 60 and 80 min. The value of band gap was found to be between 2.23 - 2.27 eV depending on deposition condition. It was observed that the band gap energy values obtained on films at different deposition time did not show any important changes; however the band gap energy increases slowly with deposition time (Figure 7b).

Morphology properties and elemental composition of CdS thin films

Scanning electron microscope (SEM) was used for the morphological study of CdS thin films. Figure 8, 9 and 10 shows the SEM images of CBD-CdS at X1000 magnification for 40, 60 and 80 min. It is observed that the films where uniform and smooth throughout all the regions which means that the deposited film was uniform yellowish and well substrate covered. The films are without pinhole or cracks, from all samples, we clearly observe the small particles tied up in a fibrous-like porous structure, this indicates the nanocrystalline nature of CdS thin films deposited.

The elemental composition of the as-deposited CdS thin film was investigated using EDAX and the pattern is shown in Figures 11, 12 and 13 for different deposition time (40, 60 and 80 min, respectively) using chemical bath deposition method. For all samples, peaks of Cd and S exhibit the presence of these elements in the deposited thin film. Also for all samples, the ratio of Cd element is more compared to S element. The peaks of silicon originate from the glass substrate.

Conclusion

The chemical bath method was successfully used to

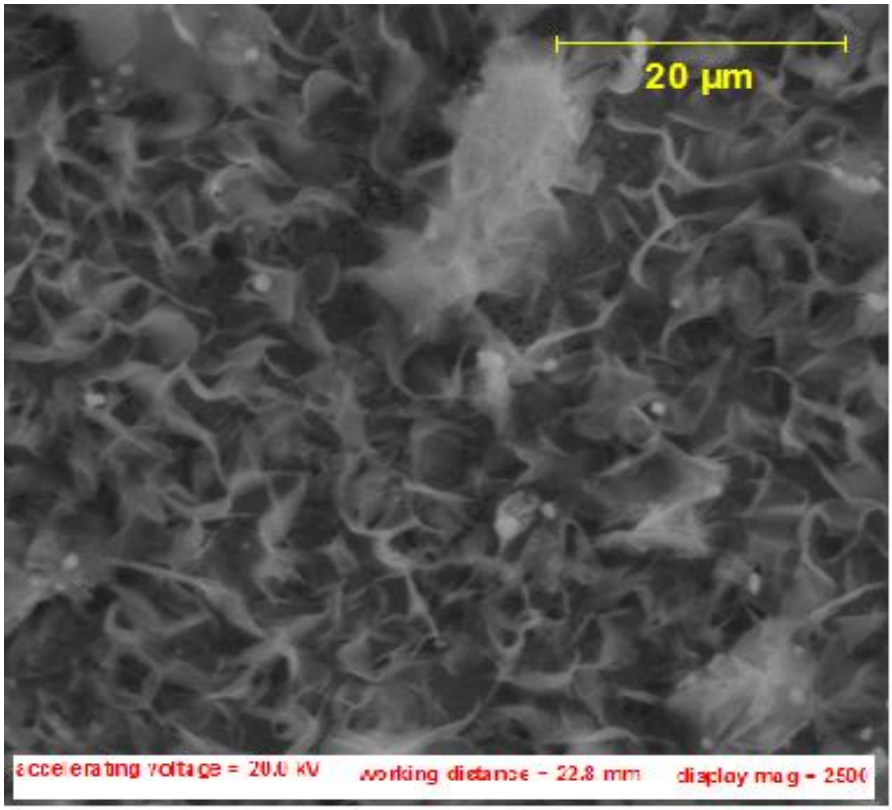

Figure 8. SEM image of CBD-CdS film 40 min.

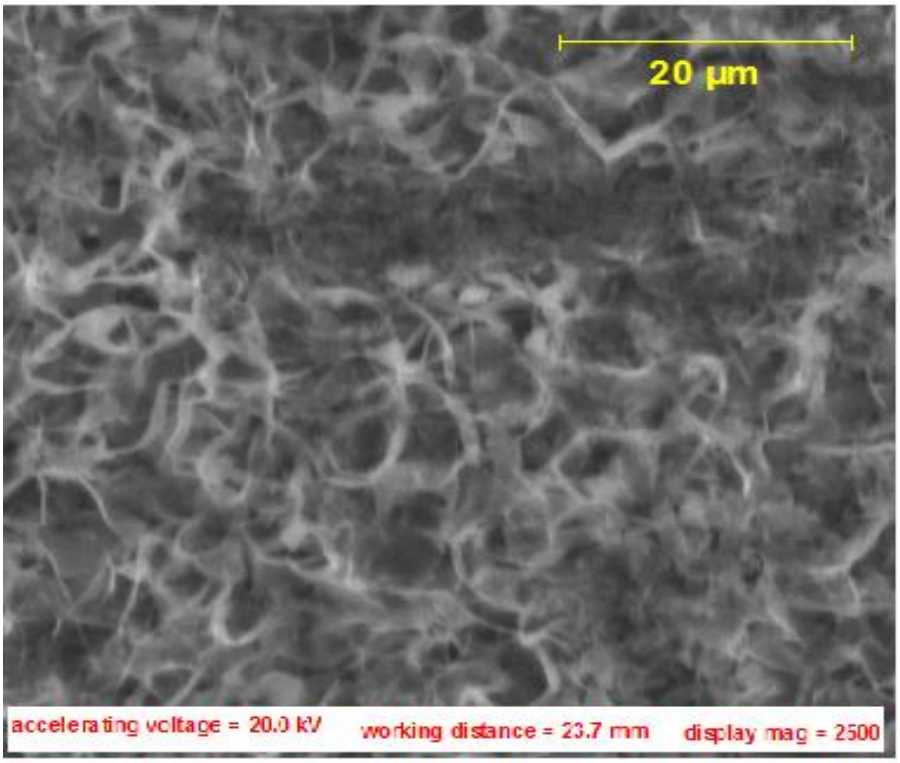

Figure 9. SEM image of CBD-CdS film 60 min.

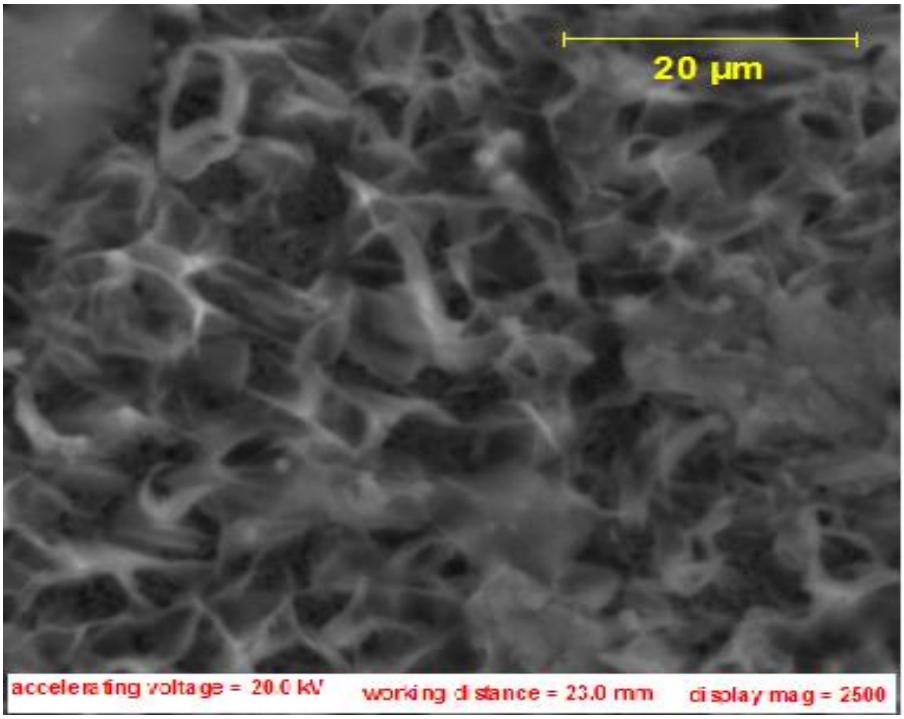

Figure 10. SEM image of CBD-CdS film 80 min.

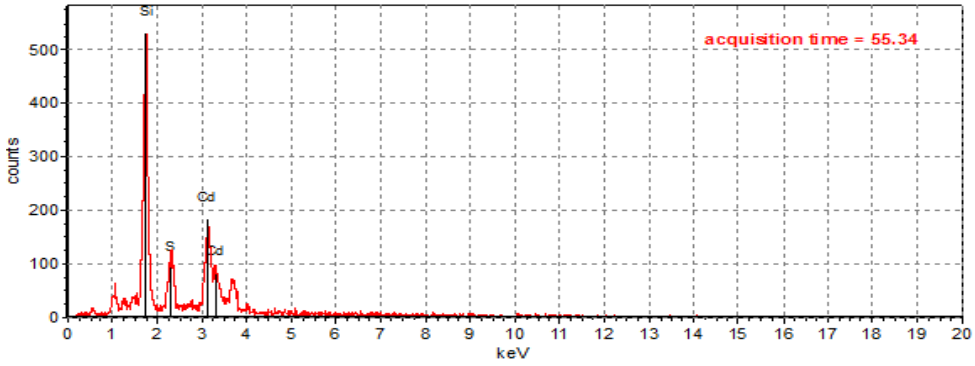

Figure 11. EDAX pattern of CBD-CdS thin film 40 min.

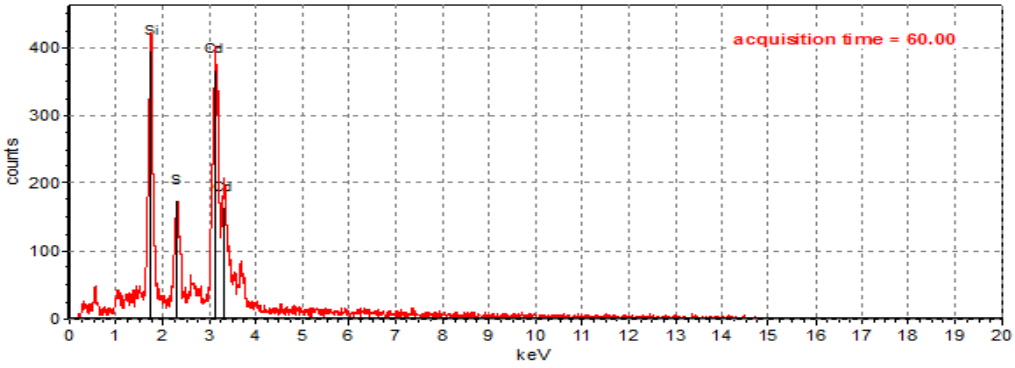

Figure 12. EDAX pattern of CBD-CdS thin film 60 min.

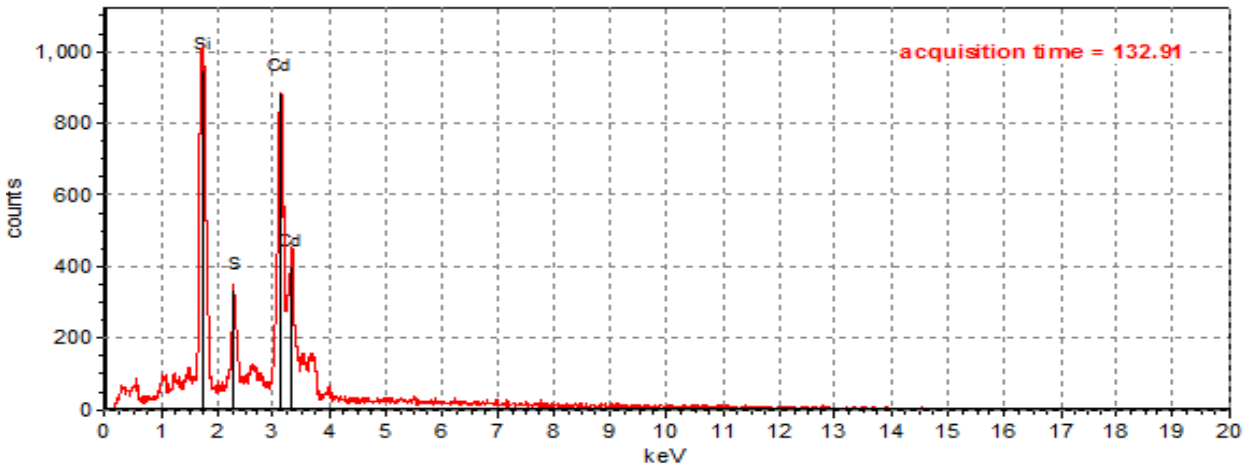

Figure 13. EDAX pattern of CBD-CdS thin film 80 min.

deposit CdS thin films. The morphology of the thin films is smooth, uniform and good adherent to substrate surface for all samples. The EDAX pattern showed the presence of Cadmium and Sulfur which was the salt used in this experiment. The prepared films were found to be nanocrystalline thin films. XRD analysis reveals that CdS thin films are polycrystalline having a hexagonal structure with a preferential orientation of (002) plane for all samples. In the optical studies, the CdS thin film showed a high absorbance and high absorbance coefficient in the area of the visible region, this makes the deposited film suitable in the designing of solar cells. The energy band gap for deposited CBD - CdS thin film was in the range of 2.23 – 2.42eV which can be used in the application of thin film as window layer in solar cell fabrication.

Conflict of Interest

The authors declare no conflict of interests.

REFERENCES

Abdullah MA, Al-Hussam S, Abdul-Jabbar J (2012). Synthesis, structure, and optical properties of CdS thin films nanoparticles prepared by chemical bath technique. J. Assoc. Arab Univ. Basic Appl. Sci. 11:27–31.

Awodugba AO, Adedokun O, Sanusi YK (2012). Study of optical and crystallographic properties Of Cbd Grown Cds Thin Films. IJRRAS. 12(3).

Awodugba AO, Adedokun O (2011). On the physical and optical characteristics of cds thin films deposited by the chemical bath deposition technique. Pacific J. Sci. Technol. 12(2):334–341.

Bastol BM, Tseng ES, Lo DS (1985). Electrodeposition of thin film heterojunction devices that utilize Cd-rich MCT. US Patent. 4:548-681.

Chamberlain RR, Skarman JS (1966). Chemical spray deposition process for inorganic films, J. Electrochem. Soc.113:86.

Demir R, Gode F (2015). Structural, optical and electrical properties of nanocrystalline CdS thin films grown by chemical bath deposition method. chalcogenide lett.12(2):43-50.

Enriquez JP, Mathew X (2003). CdTe/CdS Solar cells on flexible molybdenum substrates. Solar Energy Mater. Solar Cells. 76:313-322.

Ezema FI, Ezugwu SC, Osuji RU, Asogwa PU, Ezekoye BA, Ekwealor ABC, Ogbu MP (2010). Role of thermal annealing on the optical and solid state properties of chemically deposited cadmium sulphide nanocrystalline thin film grown in a polymer matrix. J. Non-Oxide Glasses. 1(1):45–50.

Fajinmi GR, Adelabu JSA (2009). Preparation and characterization of chemically deposited cadmium sulphide thin films. Pacific J. Sci. Technol. 10:817-822

Fangyang L, Yanqing L, Jun L, Bo W, Sanshuang K, Zhian Z, Jie L, Yexiang L (2010). Characterization of chemical bath deposited CdS thin films at different deposition temperature. J. Alloys Compounds. 493:305–308.

Gopinathan C, Sarveswaran T, Mahalakshmi K, Saravanakumar K (2011). Studies on CdS Nanocrystalline thin films with different S/Cd ratios prepared using chemical bath deposition method. Adv. Studies Theor. Phys. 5(4):171–183.

Jadhav UM, shinde MS, Patel SN, Patil RS (2014). Structural, optical and electrical properties of nanocrystalline cadmium sulphide (CdS) thin films deposited by novel chemical route. Indian J. pure appl. Phys. 52:39-43.

Kodigala SR, Pilkington RD, Hill AE, Tomlinson RD, Bhatnagar AK (2001). Structural and optical investigations on CdS thin films grown by chemical bath technique. Mater. Chem. Phys. 68:22–30.

Liu QQ, Shi JH, Li ZQ, Zhang DW, Li XD, Sun Z, Zhang LY, Huang SM (2010). Morphological and stoichiometric study of chemical bath deposited CdS films by varying ammonia concentration. Physica B. 405:4360–4365.

Maeng JK, Sung HL, Sang HS (2011). Physical properties of CdS thin films grown by chemical bath deposition with directly immersed ultrasonication module. Thin Solid Films 519:1787–1793.

Mane RS, Lokhande CD (2000). Chemical deposition method for metal chalcogenide thin films. Mater. Chem. Phys. 65:1.

Mahdi MA, Kasem SJ, Hassen JJ, Swadi AA, Ani SK (2009). Structural and optical properties of chemical deposition CdS thin films. Int. J. Nanoelectronics Mater. 2:163-172.

Mathew M (2009). Engineering the properties of indium sulfide for thin film solar cells by doping. Ph.D. thesis Cochin Univ. Sci. Technol. pp.1-2.

Moualkia H, Hariech S, Aida MS (2009). Structural and optical properties of CdS thin films grown by chemical bath deposition. Thin Solid Films. 518:1259.

Oliva-Avilés AI, Patino R, Oliva AI (2010). CdS films deposited by chemical bath under rotation. Appl. Surface Sci. 256:6090–6095.

Partha PC, Ayan M (2014). Synthesis of Nanocrystalline CdS by SILAR

and their characterization. P. Mitra Hindawi Publishing Corporation J. Mater. Article ID 138163:1-6.
Selma MH, Al-Jawad A, Mousa M, Wessal AT (2009). Investigation of optical properties of cadmium sulfide (CdS) thin films by chemical bath deposition. Um-Salama Sci. J. 6(1).
Ximello-Quiebras JN, Contreras-Puente G, Aguilar-Hern!andez J, Santana-Rodriguez G, Arias-Carbajal Readigos A (2004). Physical properties of chemical bath deposited CdS thin films, Solar Energy Mater. Solar Cells. 82:263–268.
Ximello-Quiebras JN, Contreras-Puente G, Rueda-Morales G, Vigil O, Santana-Rodriguez G, Morales-Acevedo A (2006). Properties of CdS thin films grown by CBD as a function of thiourea concentration. Solar Energy Mater. Sol. Cells. 90:727.

International Journal of Physical Sciences